Simulating supermassive black hole mass measurements for a sample of ultra massive galaxies using ELT/HARMONI high spatial resolution integral-field stellar kinematics

Dieu D Nguyen, Michele Cappellari, Miguel Pereira-Santaella

Monthly Notices of the ROYAL ASTRONOMICAL SOCIETY

MNRAS **526,** 3548–3569 (2023) https://doi.org/10.1093/mnras/stad2860
Advance Access publication 2023 October 12

Simulating supermassive black hole mass measurements for a sample of ultramassive galaxies using ELT/HARMONI high-spatial-resolution integral-field stellar kinematics

Dieu D. Nguyen [1]★ Michele Cappellari [2] and Miguel Pereira-Santaella [3]

[1] *Université de Lyon 1, ENS de Lyon, CNRS, Centre de Recherche Astrophysique de Lyon (CRAL) UMR5574, F-69230 Saint-Genis-Laval, France*
[2] *Sub-Department of Astrophysics, Department of Physics, University of Oxford, Denys Wilkinson Building, Keble Road, Oxford OX1 3RH, UK*
[3] *Instituto de Física Fundamental, CSIC, Calle Serrano 123, E-28006 Madrid, Spain*

Accepted 2023 September 14. Received 2023 September 14; in original form 2023 February 21

ABSTRACT

As the earliest relics of star formation episodes of the Universe, the most massive galaxies are the key to our understanding of the stellar population, cosmic structure, and supermassive black hole (SMBH) evolution. However, the details of their formation histories remain uncertain. We address these problems by planning a large survey sample of 101 ultramassive galaxies ($z \leq 0.3$, $|\delta + 24^\circ| < 45^\circ$, $|b| > 8^\circ$), including 76 per cent ellipticals, 17 per cent lenticulars, and 7 per cent spirals brighter than $M_K \leq -27$ mag (stellar mass $2 \times 10^{12} \lesssim M_\star \lesssim 5 \times 10^{12}$ M$_\odot$) with ELT/HARMONI. Our sample comprises diverse galaxy environments ranging from isolated to dense-cluster galaxies. The primary goals of the project are to (1) explore the stellar dynamics inside galaxy nuclei and weigh SMBHs, (2) constrain the black hole scaling relations at the highest mass, and (3) probe the late-time assembly of these most massive galaxies through the stellar population and kinematical gradients. We describe the survey, discuss the distinct demographics and environmental properties of the sample, and simulate their HARMONI I_z-, $I_z + J$-, and $H + K$-band observations by combining the inferred stellar-mass models from Pan-STARRS observations, an assumed synthetic spectrum of stars, and SMBHs with masses estimated based on different black hole scaling relations. Our simulations produce excellent state-of-the-art integral field spectrography and stellar kinematics ($\Delta V_{\rm rms} \lesssim 1.5$ per cent) in a relatively short exposure time. We use these stellar kinematics in combination with the Jeans anisotropic model to reconstruct the SMBH mass and its error using a Markov chain Monte Carlo simulation. Thus, these simulations and modellings can be benchmarks to evaluate the instrument models and pipelines dedicated to HARMONI to exploit the unprecedented capabilities of ELT.

Key words: galaxies: general – galaxies: supermassive black holes – galaxies: kinematics and dynamics – galaxies: nuclei – galaxies: evolution – galaxies: formation.

1 INTRODUCTION

Supermassive black holes (SMBHs) discovered at the centres of massive galaxies ($10^{10} < M_\star \lesssim 2 \times 10^{11}$ M$_\odot$) have masses ($M_{\rm BH}$) correlating with the galaxy's macroscopic properties. These $M_{\rm BH}$ scaling relations include the galaxy luminosity (e.g. L_K or L_V; Kormendy & Richstone 1995), the stellar mass of the galactic bulge component ($M_{\rm bulge}$) or the stellar mass of the entire galaxy ($M_\star$; e.g. Magorrian et al. 1998), the stellar bulge velocity dispersion ($\sigma_\star$; e.g. Ferrarese & Merritt 2000; Gebhardt et al. 2000), the circular velocity of the extended H I rotation curves ($v_{\rm c}$; e.g. Ferrarese 2002; Sun et al. 2013), the velocity width of circumnuclear molecular gas discs (ΔV; Smith et al. 2020), and the galaxy concentration (e.g. Graham et al. 2001, 2003). The tightness and dynamic range covering several orders of magnitude of these correlations indicate that the evolution of these objects is closely linked (e.g. Kormendy & Ho 2013; McConnell et al. 2013; Saglia et al. 2016; van den Bosch 2016, hereafter V16; Sahu, Graham & Davis 2019a, b; Greene, Strader & Ho 2020). Thus, understanding the shapes, related scatters, and the universality of such correlations will reveal the physical processes involved in the growth of black holes and galaxies.

Investigations from the demographics of known galaxies hosting SMBHs have demonstrated the non-universality of the $M_{\rm BH}$–galaxy scaling relations (e.g. Sahu et al. 2019a; Greene et al. 2020), e.g. galaxies with active galactic nuclei (AGN; e.g. Chilingarian et al. 2018), masers (e.g. Greene et al. 2010), bars (e.g. Graham & Spitler 2009), pseudo-bulges (e.g. Gültekin et al. 2009), or late-type spirals (LTGs; e.g. Greene et al. 2016; Läsker et al. 2016) that are almost below the same relations of more massive counterparts interpolated towards the low-mass regimes of both SMBHs and host galaxies (e.g. Nguyen et al. 2014, 2017, 2018, 2019; Nguyen 2017, 2019).

Additionally, examinations of the variation of $M_{\rm BH}$ function in the mass–size diagram of the stellar mass ($M_\star$) and effective radius ($R_{\rm e}$, the radius that encloses the half-light of the galaxy) suggest various growth pathways (Cappellari 2016, hereafter C16; Krajnović, Cappellari & McDermid 2018a, hereafter K18). For example, numerous galaxy properties, such as $\sigma_\star$, mass-to-light ratio (M/L), gas content, bulge fraction, stellar population, and morphology, vary systematically along the lines of $R_{\rm e} \propto M_\star$, where $\sigma_\star$ = constant (fig. 23 of

★ E-mail: nddieuphys@gmail.com

C16). The same variation along the lines of constant $\sigma_\star$ happens for $M_{\rm BH}$ (fig. 1 of K18). This $M_{\rm BH}$ transition occurs along the lines of constant $\sigma_\star$ for galaxies that have $M_\star$ less than a critical mass $M_{\star,\rm crit} \approx 2 \times 10^{11}$ M$_\odot$, suggesting the primary growth of both SMBHs and host galaxies via cold gas accretion, gas-rich minor mergers, and secular evolution predicted by the current well-established $M_{\rm BH}$–galaxy scaling relations (e.g. Kormendy & Ho 2013).

However, one finds evidence for a change in the $M_{\rm BH}$ variation in galaxies that are more massive than this critical mass located at the opposite ends of the $M_{\rm BH}$–galaxy scaling relations (McConnell & Ma 2013). Their $M_{\rm BH}$ are positive outliers from the $M_{\rm BH}$–$L_{K,\rm bulge}$ and $M_{\rm BH}$–$M_{\rm bulge}$ relations (McConnell & Ma 2013; Walsh et al. 2015, 2016, 2017), the $M_{\rm BH}$–$\sigma_\star$ relation (C16; V16; K18), or the correlation of the $M_{\rm BH}$–host galaxy's core break radius ($r_{\rm b}$) inferred from the galaxy's core-Sérsic surface-brightness profile (also known as the $M_{\rm BH}$–$r_{\rm b}$ relation; Rusli et al. 2013; Dullo 2019), which is used to describe the morphology of the most massive galaxy (see Section 4.3) approximately one order of magnitude of $M_{\rm BH}$. The $M_{\rm BH}$–$\sigma_\star$ (McConnell & Ma 2013) correlation and the $M_\star$–$R_{\rm e}$ diagram (K18), which includes the four brightest cluster galaxies (BCGs; McConnell & Ma 2013), start to depart from their same correlations without having these four BCGs around the mass of $M_\star \approx 3 \times 10^{10}$ M$_\odot$ (C16). This suggests that massive galaxies assemble their matter, changing from a sequence of bulge growth to dry-merger growth (Krajnović et al. 2013), predominantly through dissipation-less equal-mass dry mergers according to current numerical simulations that linearly increase $M_{\rm BH}$, $R_{\rm e}$, $r_{\rm b}$, and $M_\star$ but not $\sigma_\star$ (e.g. Boylan-Kolchin, Ma & Quataert 2006; Naab & Ostriker 2017).

Recent progress in looking for the best scaling relation and its universal indication of possible formation mechanisms starts with the two-channel-formation paradigm of galaxies, assuming that SMBHs and hosts evolve simultaneously affected by the galaxy stellar mass and environment (e.g. Peng et al. 2010, K18). This idea was motivated by both theoretical (Oser et al. 2010) and observational (Cappellari 2013; van Dokkum et al. 2015) evidence (see also the review in C16). To test this hypothesis, we consider the distribution of galaxies with $M_{\rm BH}$ measurements in the $M_\star$–$R_{\rm e}$ diagram (Cappellari et al. 2013b) to find the most massive galaxies ($M_\star > 10^{12}$ M$_\odot$) located at the top of the galactic-mass ladder. Therefore, we search for evidence of the growing dependence of $M_{\rm BH}$ with galaxy properties moving from $\sigma_\star$ to $M_\star$ in the highest-mass targets (Scott et al. 2013). In other words, to understand which of the correlations ($M_{\rm BH}$–$\sigma_\star$ versus $M_{\rm BH}$–$M_\star$) is more fundamental and a better predictor of $M_{\rm BH}$ in the highest-galaxy-mass regime, more systemic $M_{\rm BH}$ measurements are needed. However, these galaxies are extremely rare in the local universe ($D_{\rm A} < 110$ Mpc), and to find them, one has to reach out to where the required spatial resolutions and sensitivities go below the limits of existing ground-based adaptive optics (AO) assisted telescopes (e.g. Gemini and the Very Large Telescope, VLT). We thus employ the Extremely Large Telescope (ELT) integral field spectrograph (IFS) to investigate the physical conditions and dynamics deep inside galaxy nuclei.

In this work, we (1) utilize the available near-infrared (NIR) photometric surveys (Section 2.1) to define a volume-limited sample of the highest-mass galaxies accessible at the ELT site, then (2) investigate the potentials of using the High Angular Resolution Monolithic Optical and Near-infrared Integral field spectrograph (HARMONI; Thatte et al. 2016, 2020) on ELT in exploring the nuclear-stellar kinematics and dynamics within the sphere of influence radii (SOI, $r_{\rm SOI} = G M_{\rm BH}/\sigma_\star^2$, where G is the gravitational constant) of SMBHs or, more likely, most massive black holes (MMBHs), then weighing their $M_{\rm BH}$ at further distances (or $M_{\rm BH}$ at high redshift) than those that could be resolved by the current apparatuses (e.g. VLT and Gemini assisted by AO). We demonstrate the ELT capabilities in spatial and spectral resolutions relative to the stringent technical requirements for direct $M_{\rm BH}$ measurements. In addition, we test the technically demanding nature of the required determinations and the limits of HARMONI and thus provide technical guidance for a wide range of studies to probe the underlying physics of galaxy and black hole coevolution.

We describe the parent sample, defining specific selected criteria to identify our MMBH survey sample, and present their essential properties in Sections 2 and 3, respectively. We describe the dynamical and photometric model that we use for our simulations in Section 4. In Section 5, we perform NIR integral field spectroscopic (IFS) simulations using the HARMONI Simulator (HSIM; Zieleniewski et al. 2015) software for ELT observations on the HARMONI instruments and demonstrate its simulated data cubes and stellar kinematics extractions. In Section 6, we discuss the potential of application for dynamical modelling to measure the masses of central black holes using these observations and their limits. We conclude our findings in Section 7.

Throughout this work, we quote all quantities using a foreground extinction correction (Schlafly & Finkbeiner 2011) and the Cardelli, Clayton & Mathis (1989) interstellar extinction law, as well as assuming a standard flat universe with the Hubble constant $H_0 \approx 70\,{\rm km\,s^{-1}\,Mpc^{-1}}$, matter density $\Omega_{\rm m,\,0} \approx 0.3$, and dark energy density $\Omega_{\Lambda,\,0} \approx 0.7$, which is consistent with the latest constraints from *Planck* (Planck Collaboration 2014) and *WMAP* (Calabrese et al. 2017). We use the AB-photometric magnitude system (Oke 1974) throughout the analysis, unless otherwise indicated in the text. All the maps presented in this article show the galaxy's major axis aligned along the horizontal direction and the galaxy's minor axis aligned along the vertical direction.

2 SAMPLE SELECTION

2.1 $K_{\rm s}$-band magnitude and distances

We utilized the photometric information provided in the NIR ($\approx$2.2 μm) $K_{\rm s}$-band luminosity by the full-sky and homogeneous photometry of the Two Micron All Sky Survey (2MASS; Skrutskie et al. 2006) redshift survey (2MRS; Huchra et al. 2012) as our parent sample to search for the most massive galaxies. The K band is 5–10 times less sensitive to dust absorption than the optical, and the M/L_K varies within a factor around two or three times smaller than the optical (Bell & de Jong 2001; Maraston 2005). Ma et al. (2014) also tested the potentially underestimated luminosity of 2MASS $K_{\rm s}$-band magnitudes in galaxy selection caused by its relatively shallow photometry (Schombert & Smith 2012) and the relatively small size of the sources themselves, making it difficult to determine accurate the Sérsic index for the light profiles. Ma et al. (2014) compared the 2MASS photometry against the *Hubble Space Telescope* (*HST*) photometry of 219 early-type galaxies (ETGs) from Lauer et al. (2007b) and found that $K_{\rm s}$-band selection does not appear to be greatly affected by potentially systematic underestimates in the 2MASS $K_{\rm s}$-band magnitude. In this work, we look for more massive targets than the MASSIVE sample (Ma et al. 2014), where this effect could be negligible. Thus, 2MRS is the best parent sample for selecting dust-poor distant bright candidates with robust stellar-mass approximations.

However, it is necessary to have distances for deriving galaxy luminosities and stellar masses from the observed apparent magnitudes. We matched approximately 100 000 galaxies that have

NASA/IPAC Extragalactic Database (NED[1]) redshift-independent distances[2] (NED-D; Steer et al. 2017) with the 2MRS galaxies but adopted their NED-D distances obtained with ≈(10–20) per cent accuracy. Otherwise, for the targets from 2MRS that do not have independent distances available, we derived distances from redshifts because, at the distances of our sample, peculiar motions due to the Virgo cluster, the Great Attractor, and the Shapley supercluster become negligible compared to the Hubble flow, making redshift distances accurate.

The 2MASS extended source (XSC) catalogue (Skrutskie et al. 2006) provides the K_s apparent magnitude (Vega system) measurements for approximately 1.6 million galaxies (*k_m_ext* XSC keyword). We converted these apparent magnitudes into absolute magnitudes, $M_K = K_T - 5\log D_L - 25 - 0.11 \times A_V$. Here, $K_T \equiv$ *k_m_ext* measured in an isophotal aperture of a single Sérsic surface-brightness profile extrapolated to the inner-unresolved profile (Jarrett et al. 2003); A_V is the Galactic extinction in the Landolt V band from Schlafly & Finkbeiner (2011) and the reddening relation of Charlot & Fall (2000) with $R_V = A_V/E(B-V) = 3.1$; and D_L is the luminosity distance.

To determine the selection criteria for galaxies in our MMBH IFS survey, we relied on (1) the nominal spatial resolution for HARMONI's image quality and resolving their SMBH r_{SOI}, (2) the minimum luminosity in the K band (M_K), and (3) the availability of a tip–tilt star near the science target (or a natural guide star, NGS) that serves as a reference in the sky to correct the atmospheric turbulence effect on the ground-based IFS.

For the first requirement, Thatte et al. (2016, 2020) argued that the intermediate spatial scale of $10 \times 10\,\mathrm{mas}^2$ is optimal because the instrument's long-exposure point spread function (PSF) with a full width at half-maximum (FWHM) of 12 mas has an ensquared energy of ≥75 per cent within a 2×2 spaxel^2 box, i.e. one spaxel = 10 mas. In practice, we wish to detect the genuinely stellar kinematic signature within the SMBH's SOI, which should stay within several spaxels at least. We started from the standard formula to estimate the black hole sphere of influence radius $r_{SOI} = GM_{BH}/\sigma_\star^2$. Given the units of Mpc for the angular-size distance (D_A[3]), $M_\odot$ for the black hole mass (M_{BH}), and km s^{-1} for the velocity dispersion ($\sigma_\star$), we obtain r_{SOI} in arcseconds:

$$r_{SOI}\,(\mathrm{arcsec}) \approx 8.87 \times 10^{-4} \left(\frac{M_{BH}}{M_\odot}\right) \left(\frac{\mathrm{Mpc}}{D_A}\right) \left(\frac{\mathrm{km\,s^{-1}}}{\sigma_\star}\right)^2. \quad (1)$$

Next, we conservatively adopt $\sigma_\star \approx 300\,\mathrm{km\,s^{-1}}$, which is a characteristic value for the most massive nearby ETGs (e.g. C16) and varies weakly with galaxy mass (Krajnović et al. 2013; Naab & Ostriker 2017). Using the M_{BH}–$\sigma_\star$ relation from equation (7) of Kormendy & Ho (2013), this $\sigma_\star$ corresponds to $M_{BH} = 1.8 \times 10^9$ $M_\odot$. Thus, the above equation becomes

$$r_{SOI}\,(\mathrm{arcsec}) \approx \frac{18.0}{D_A}. \quad (2)$$

Finally, we require the spatial scale of $r_{SOI} \approx 20$ mas for our MMBH IFS survey, which is well sampled by two 10 mas HARMONI spaxels in radius (discussed later in Section 5.2), or equivalently we have $\pi \times (20/10)^2 \approx 12$ spaxels inside the sphere of influence. Given this resolving scale and equation (2), the distance limit should be $D_A \approx 902$ Mpc. Since we define our selection based on observable redshift rather than D_A, we thus round our redshift selection to $z = 0.3$, which corresponds to a slightly larger $D_A \approx$ 950 Mpc in the adopted standard cosmology.

We should note that this choice of $r_{SOI} \approx 20$ mas in our survey is a lower limit for the following reasons: (i) we expect that the central black holes in our MMBH survey are MMBHs, much larger than the predictions from the Kormendy & Ho (2013) M_{BH}–$\sigma_\star$ relations of the nearby and smaller-mass galaxies, and (ii) we put the galaxies at the furthest D_A of the sample.

For the second requirement, we chose candidates brighter than $M_K \leq -27.0$ mag to search for ultramassive galaxies. This M_K limit roughly corresponds to a B-band selection $M_B \lesssim -24.7$ mag for the typical $B - K_s \approx 2.5$ mag colour at the faint end of our selected sample. To give a sense of the extreme masses of our selected galaxies, we note that the BCG NGC 4889 of the Coma cluster is the brightest galaxy within the local $D \lesssim 100$ Mpc volume, with a magnitude $M_K = -26.6$ mag (Cappellari 2013).

Finally, we take into account the third requirement by examining the available images on the Panoramic Survey Telescope and Rapid Response System (Pan-STARRS), Sloan Digital Sky Survey (SDSS), and 2MASS archival data base in multiple bands (e.g. r, g, and i) for target galaxies passing the first and second requirements above. Our main purpose is to search for tip–tilt stars that can be used as reference stars in the vicinity sky to correct the atmospheric disturbances on the ground-based IFS by applying the laser tomography adaptive optics (LTAO) mode when using the HARMONI instrument (see Section 5.2). We should note that 2MASS and Pan-STARRS lack the spatial resolution to identify such stars; we thus rely on SDSS only for finding tip–tilt stars. However, the sky coverage of SDSS does not match the ELT's observability. We, therefore, do not push this third observational requirement to be as strong as the first two conditions during the MMBH sample selection in this work.

Ideally, these NGS should be off the target galaxies' centres by about (12–60) arcsec and have limiting magnitude in the H band of <19 mag in the Vega magnitude system (or <20.4 AB mag). For some NGS that do not have available H-band apparent magnitudes but do have Sloan values, we first made a correction to convert the SDSS magnitude system (i.e. Asinh magnitude) to conventional magnitudes, although the difference between the Asinh and conventional magnitudes is <1 per cent for objects brighter than Asinh magnitude $m(f/f_0) = 22.12, 22.60, 22.29, 21.85, 20.32$ for *ugriz* (Lupton, Gunn & Szalay 1999), where f/f_0 = (counts/exposure time) $\times$ $10^{0.4 \times (\text{photometric zeropoint} + \text{extinction coefficient} \times \text{airmass})}$. Secondly, we converted the SDSS magnitude system to AB magnitudes: $ugriz(AB) = 22.5 - 2.5 \times \log_{10} f_{ugriz} - q$, where $q = 0.042, 0.036, 0.015, 0.013, 0.002$ for *ugriz*. Thirdly, we transformed the SDSS AB magnitude to the 2MASS (i.e. JHK_s) AB magnitude using equation (4) and information in table 5 of Bilir et al. (2008). We find that 90 per cent of the galaxies in our MMBH sample have available SDSS imaging. Out of these, 80 per cent satisfy this tip–tilt star requirement for LTAO correction. We assume that a similar fraction will apply to the whole MMBH sample.

2.2 Selection criteria

We thus enforced obvious observability criteria and described the following selection steps:

[1] https://ned.ipac.caltech.edu/

[2] http://ned.ipac.caltech.edu/Library/Distances/

[3] Because this MMBH survey targets the most massive galaxies that possibly host MMBHs beyond the local universe, their redshifts become critical. It is thus necessary to distinguish the luminosity distance (D_L) and the angular-size distance (D_A). While we use D_L to estimate M_K and $M_\star$ only, D_A has to be used to define the r_{SOI} of central black holes. We thus quote them with careful indications throughout this article.

Table 1. Target selection criteria.

Redshift	$z \leq 0.3$
Galaxy total magnitude	$M_K \leq -27.0$ mag
Observability	$\lvert\delta + 24^\circ\rvert < 45^\circ$
Galaxy zone of avoidance	$\lvert b\rvert > 8^\circ$
Tip–tilt stars[a]	(12–60) arcsec away from the target's centre $m_H < 19$ Vega mag (or < 20.4 AB mag)

[a]The laser tomography adaptive optics (LTAO) mode on the ELT/HARMONI instrument needs at least one natural guide star (NGS) to work simultaneously with six other artificial off-axis laser guide stars (LGS). The system causes the required NGS to be more than 10 000 times fainter than that from the classical AO used on Gemini and VLT. In this work, we use the first four criteria listed above for selecting the MMBH survey members (Table 2). The tip–tilt star requirement is used to access a high likely fraction of the MMBH sample only where we can find a few suitable NGS using the available data bases from SDSS (i.e. 2MASS and Pan-STARRS lack the spatial resolution to identify such stars) because the sky coverage of SDSS does not match the ELT's observability.

Table 2. Main characteristics of the MMBH IFS survey sample.

Angular-size distance	$136 < D_A \leq 950$ Mpc
Luminosity distance	$145 < D_L \leq 1600$ Mpc
K_s-band luminosity	$L > 1.3 \times 10^{12}$ L$_{\odot K}$
Total stellar mass	$2 \times 10^{12} \lesssim M_\star \lesssim 5 \times 10^{12}$ M$_\odot$
B-band absolute magnitude	$M_B \lesssim -24.7$ mag
Number of galaxies in the sample	$N_{gal} = 101$
Number of ellipticals ($T \leq -3.5$)	77 (≈76 per cent)
Number of lenticulars ($-3.5 < T \leq -0.5$)	17 (≈17 per cent)
Number of spirals ($-0.5 < T \leq 8$)	7 (≈7 per cent)

Notes. The galaxy Hubble type (T) is defined using HyperLeda: http://leda.univ-lyon1.fr/search.html. The survey volume removed the Milky Way exclusion zone and the declination selection.

(i) We expanded the explored volume out to $z \leq 0.3$, corresponding to $D_A \leq 950$ Mpc and $D_L \leq 1600$ Mpc for the brightest targets that satisfy $M_K \leq -27.0$ mag. These selected targets are even more massive than the current sample of MUSE Most Massive Galaxies (M3G, $-26.7 \leq M_K < -25.7$ mag; Krajnović et al. 2018b).

(ii) We tightened the specific observability criterion based on the location of ELT on the top of Mount Cerro Armazones in the Atacama Desert of northern Chile and the limit on the zenith distance for a good AO correction: $\lvert\delta + 24^\circ\rvert < 45^\circ$, where δ is the sky declination (Thatte, private communication).

(iii) We excluded the galactic equatorial plane and galactic bulge regions, highly contaminated by dust: $\lvert b\rvert \leq 8^\circ$, where b is the Galactic latitude.

(iv) We checked for existing NGS stars with $m_H < 19$ Vega mag (or < 20.4 AB mag) that should be at distances between (12–60) arcsec away from the science target's centre. However, due to the lack of spatial resolution and the difference in sky observability among the data bases that we used to find for NGS, we do not treat this criterion (iv) as having the same priority as criteria (i), (ii), and (iii).

A brief summary of the selection criteria is given in Table 1, while some general properties of our MMBH-selected sample are shown in Table 2. Fig. 1 illustrates the parameter space of D_A versus M_K of galaxies, showing that the big jump in HARMONI resolving power now allows us to open the explored comoving volume up to 1 Gpc^3 when ignoring the declination limit.

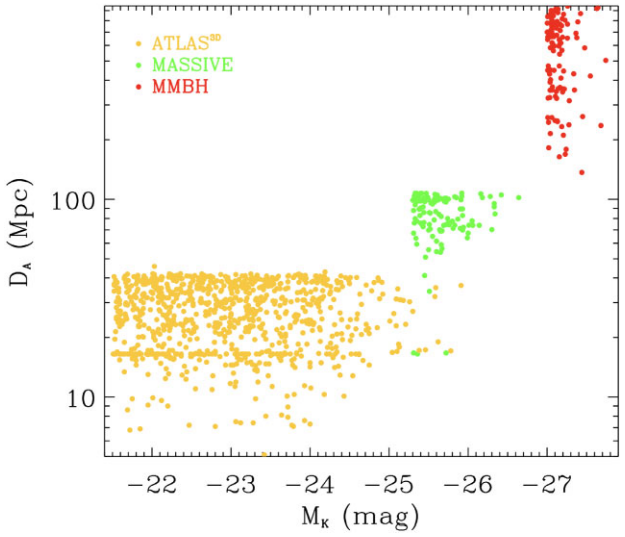

Figure 1. Angular-size distance (D_A) and absolute K_s-band magnitude (M_K) of our most massive black holes (MMBH) survey (red; this work), the MASSIVE survey (green; Ma et al. 2014), and the ATLAS^{3D} survey (yellow; Cappellari et al. 2011). There is no overlap of our MMBH sample with the two others in these parameter spaces. We assumed $D_L \approx D_A$ (see footnote 3) for the ATLAS^{3D} and MASSIVE surveys due to their low redshifts ($z < 0.025$).

3 PROPERTIES OF THE SELECTED SAMPLE

3.1 Stellar mass and size

The galaxy photometric stellar masses are estimated from the total K_s-band absolute magnitudes (extinction-corrected) using the relation in which both quantities are related to each other according to the prescription from equation (2) of Cappellari (2013) calibrated from 260 ATLAS^{3D} ETGs: $\log(M_\star) = 10.58 - 0.44 \times (M_K + 23)$. On the other hand, the source sizes are defined by $R_e = 1.61 \times j\_r\_eff$, where j_r_eff is the 2MASS XSC keyword for the semimajor axis of the isophote enclosing half of the total galaxy light in the J band (Cappellari 2013). The usage of j_r_eff instead of k_r_eff is because the J band has a better signal-to-noise ratio (S/N) than the equivalent K_s band (Cappellari et al. 2013a, K18).

Fig. 2 highlights the distinct parameter space in stellar masses and sizes occupied by our MMBH survey. The larger surveying volume from the highest redshift of MASSIVE ($z \approx 0.026$) to our adopted redshift ($z \leq 0.3$) allows us to sample the galaxy-mass function at $2 \times 10^{12} \lesssim M_\star \lesssim 5 \times 10^{12}$ M$_\odot$ for large galaxies with angular size $10 < R_e < 60$ kpc. Given no mass overlap, about half of our MMBH-selected galaxies have similar R_e with MASSIVE galaxies. Thus, our MMBH sample is the extreme mass and size complementary to ATLAS^{3D} (Cappellari 2013), MaNGA (Bundy et al. 2015), SAMI (Croom et al. 2021, third and final data release), and MASSIVE (Ma et al. 2014) in the galaxy-hierarchical structure.

3.2 Shapes

It is well established that low-mass elliptical galaxies appear to be fast rotators characterized by higher ellipticities, whereas giant ellipticals are slow rotators and are round or mildly triaxial (Kormendy & Bender 1996, C16). These facts indicate strong correlations among the shapes, kinematics, and masses of massive ETGs. It is, therefore,

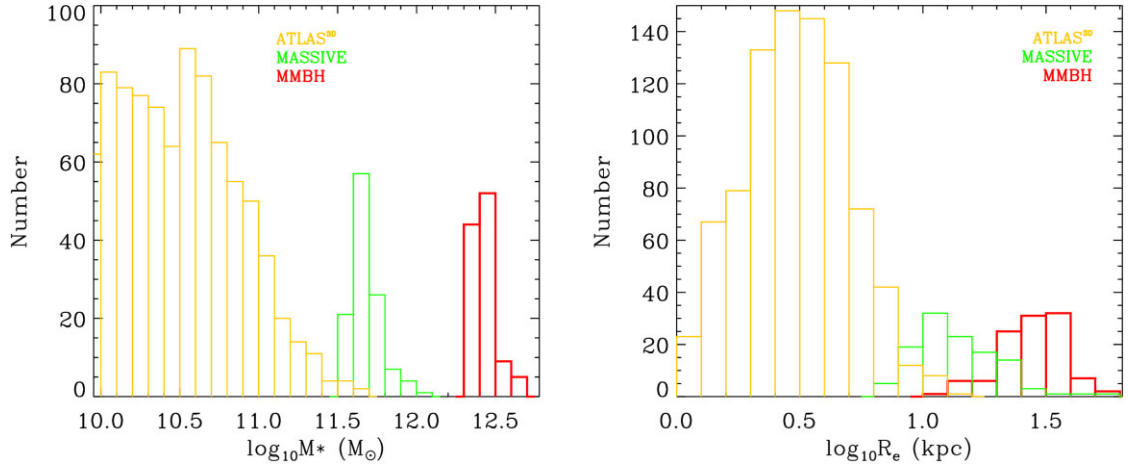

Figure 2. Distributions of stellar masses estimated from 2MASS photometry (left) and half-light radii (right) for our MMBH (red; this work), MASSIVE (green; Ma et al. 2014), and ATLAS^{3D} (yellow; Cappellari et al. 2011) galaxies.

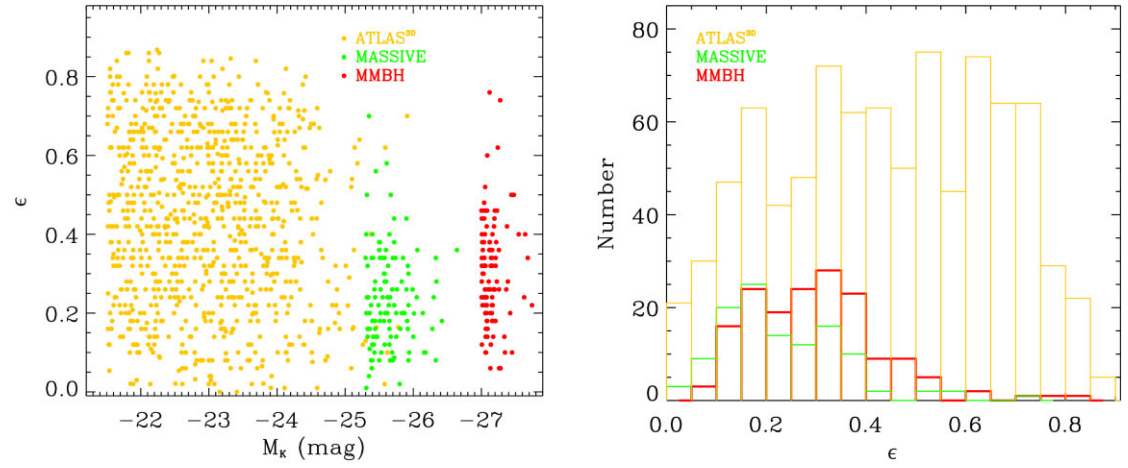

Figure 3. Ellipticity ($\epsilon = 1 - sup\_ba$) versus K_s-band luminosity (left) and ellipticity distribution (right) for our MMBH survey (red) in comparison with the MASSIVE survey (green; Ma et al. 2014) and ATLAS^{3D} (yellow; Cappellari et al. 2011).

interesting to examine the distributions in galaxy shapes for our MMBH survey.

The left-hand panel of Fig. 3 compares the ellipticity, $\epsilon = 1 - sup\_ba$, of our MMBH survey to that of MASSIVE and ATLAS^{3D}, where sup_ba is the 2MASS XSC parameter for the minor-to-major axis ratio fit to their '3σ supercoadd isophote'. Only five galaxies in each of the MASSIVE and MMBH samples have $\epsilon > 0.5$, and that is about a quarter of ATLAS^{3D} because the ellipticities are generally larger at larger radii, implying that sup_ba measured at the outermost isophote is likely an upper limit to the effective ellipticity (ϵ_e) used (Cappellari 2013). These galaxies are all in the fainter tails of $M_K < -25.7$ mag for MASSIVE and $M_K < -27.0$ mag for ours, respectively. There are depletions of high-ϵ galaxies in both samples, consistent with the fact that most of the galaxies are slow rotators for which C16 (fig. 13) adopts an empirical separation at $\epsilon \approx 0.4$. Generally, some massive galaxies have ellipticity larger than this limit because 2MASS measures the ellipticity radii larger than the half-light radius used to define ϵ_e. Moreover, the ellipticity of massive galaxies generally increases with radius. Our MMBH survey will provide direct measurements of the spatial profile of the nuclear-stellar kinematics (also ionized gas, if detected) of each galaxy and will allow us to quantify the distributions of galaxy rotations and shapes at the highest masses.

3.3 Supermassive black holes

None of the galaxies in our MMBH sample have published M_{BH} as they are located at farther distances beyond the current telescopes' resolving powers. Considering within our sample's D_A range only, 10 smaller galaxies ($M_\star \lesssim 10^{12}$ M$_\odot$ and $R_e \leq 10$ kpc) have M_{BH} measurements in the literature, mostly using the reverberation mapping emissions from the broad-line regions and the dynamics of maser spots (table 2 of V16), but they did not pass the selection criteria (Table 1). Amongst these measurements, only two BGCs satisfied our observability criteria but were located high in the Northern sky. These galaxies and their SMBHs occupy the high-mass ends and also have a large scatter on the M_{BH}–$\sigma_\star$ relation where there is a mix of very massive and lower-mass galaxies, raising concerns that the black hole–galaxy scaling relation starts changing from M_{BH}–$\sigma_\star$ to M_{BH}–$M_\star$ if we were to push to the higher-mass regime (McConnell et al. 2013). The MASSIVE survey extended the ATLAS^{3D} sample to the parameter space of $D < 110$ Mpc and $M_\star < 10^{12}$ M$_\odot$ (Ma

et al. 2014). Our MMBH survey with ELT/HARMONI will thus complement $M_{\rm BH}$ in the highest-mass galaxies ($2 \times 10^{12} \lesssim M_\star \lesssim 5 \times 10^{12}$ M$_\odot$) that locate at further distances ($136 < D_{\rm A} \leq 950$ Mpc or $145 < D_{\rm L} \leq 1600$ Mpc) and very likely host MMBHs, predicted by equation (3) of K18.

3.4 Black hole–galaxy scaling relations

Efforts in IFS-kinematic data and modelling developments in the past several years have substantially increased the number of dynamical measurements of $M_{\rm BH}$ in very high-mass galaxies (Rusli et al. 2011; McConnell et al. 2011a, b, 2012; van den Bosch et al. 2012; McConnell & Ma 2013; Walsh et al. 2013), suggesting a possible offset above the current well-established scaling relations of lower-mass galaxies (≈1 order of magnitude of $M_{\rm BH}$; e.g. Walsh et al. 2016). Nevertheless, these IFS-kinematics and modellings also caused difficulty in discriminating the models for the galaxy–black hole coevolution (Peng 2007; Hirschmann et al. 2010; Jahnke et al. 2011; Anglés-Alcázar, Özel & Davé 2013). Moreover, accurate determinations of the intrinsic scatter and the high-mass $M_{\rm BH}$ distribution is crucial for a tight constraint on $M_{\rm BH}$ function in quiescent galaxies (Lauer et al. 2007a, b), black hole demographics, the merging rate of SMBH binaries (e.g. van Haasteren et al. 2011), and the contribution of the gravitational wave background detected by the current pulsar timing experiments (Demorest et al. 2013; Shannon et al. 2013) or LISA (e.g. Gourgoulhon et al. 2019) in the future. Also, the hints of $M_{\rm BH}$ dependence in the scaling relation had changed from $\sigma_\star$ to $M_\star$ (e.g. Kormendy & Ho 2013; McConnell et al. 2013) in the highest-mass galaxies. This change indicates that the most massive galaxies grow mainly from dry mergers, distinguished from a sequence of bulge growth of the lower-mass galaxies (e.g. C16; K18) predicted by current numerical simulations (Naab & Ostriker 2017). A systemic survey of dynamical $M_{\rm BH}$ measurements in this MMBH survey without using the current scaling relations is necessary to progress our knowledge of black hole–galaxy coevolution.

Our MMBH sample comprises a significant fraction of core galaxies without central excess light profiles within a few central kiloparsecs as a signature of black hole scouring (Begelman, Blandford & Rees 1980). They are the best laboratory to investigate the scaling relations between the core and the nuclear-galaxy structure relating to the tangential stellar orbits (Kormendy & Bender 2009; Rusli et al. 2013; Thomas et al. 2014).

3.5 Uniqueness of our MMBH sample on the $M_\star$–$R_{\rm e}$ diagram

We created a mass–size diagram ($M_\star$–$R_{\rm e}$) from the 2MRS sources before applying the selection criteria and show it in Fig. 4. At low mass ($M_\star < M_{\rm crit} \approx 2 \times 10^{11}$ M$_\odot$), the lines of constant $\sigma_\star$ (and also the lines of constant $M_{\rm BH}$) trace the mass concentration and the mass density (or bulge mass fraction) of galaxies, implying that their central $M_{\rm BH}$ behave similarly with other galaxy properties. SMBH evolution thus links to optical colour, molecular-gas fraction, dynamical M/L, initial mass function (IMF) normalization, age, metallicity, and α-element abundance (fig. 22 of C16), especially their $M_{\rm BH}$ growth following the same trend as galaxy properties arising from star formation within the host galaxies (Graham et al. 2018).

Next, we applied our target selection criteria in Section 2.2 (Table 1) to the 2MRS sources on the $M_\star$–$R_{\rm e}$ diagram and plotted our MMBH-selected sample at the highest $M_\star$, $R_{\rm e}$, and $\sigma_\star$ in Fig. 4. Given their highest $M_\star$ and $\sigma_\star$, the $M_{\rm BH}$ predicted by the $M_{\rm BH}$–$\sigma_\star$ relations (equation 2 of K18) differ by more than an order of magnitude from

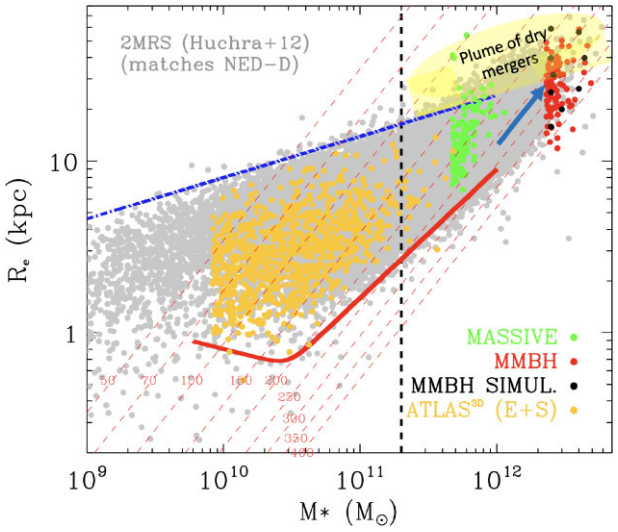

Figure 4. The mass–size diagram of 2MRS sources (grey dots) is shown in the stellar-mass range of $10^9 < M_\star < 7 \times 10^{12}$ M$_\odot$ only. The inclined red dashed lines are the constant-velocity dispersions (constant $\sigma_\star$) ranging from 50–400 km s^{-1}. The ATLAS$^{\rm 3D}$ (yellow dots; Cappellari et al. 2011, full sample of ellipticals + spirals), MASSIVE (green dots; Ma et al. 2014), and our MMBH (red and black dots; this work) galaxy surveys occupy different regions of the diagram. The thick solid red curve defines the zone of exclusion (ZOE) described by equation (4) of Cappellari et al. (2013b) in the previously explored stellar-mass range of $6 \times 10^9 < M_\star < 1 \times 10^{12}$ M$_\odot$, while the thick blue arrow indicates the qualitative growth along constant $\sigma_\star$ for dry mergers. The thick dash–dotted blue line shows the relation $(R_{\rm e}/{\rm kpc}) = 8 \times [M_\star/(10^{10}\,{\rm M}_\odot)]^{0.24}$, which provides a convenient approximation for the lowest 99 per cent contour for the distribution of ETGs (Cappellari et al. 2013b). The vertical dashed black line is the characteristic mass at $M_{\rm crit} \approx 2 \times 10^{11}$ M$_\odot$. The yellow-shaded region at the top end of the highest-mass regime (above the blue arrow) shows the signature of multiple dry-merger 'plumes' in the current data. This is a prediction from theoretical models (see fig. 29 of C16), confirmed by these data. Black dots are our MMBH galaxies selected for the HSIM IFS simulation in Section 5.2.

that predicted by equation (3) of K18, where $M_{\rm BH}$ starts following the $M_{\rm BH}$–$M_\star$ relation when $M_\star > M_{\rm crit}$. We also added the ATLAS$^{\rm 3D}$ and MASSIVE galaxies in Fig. 4 to demonstrate the uniqueness of our highest-mass galaxy sample.

One can see in Fig. 4 a 'plume' (indicated by the yellow shaded region above the blue arrow) of galaxies with sizes larger than the extrapolation of the upper boundary of the ($M_\star$, $R_{\rm e}$) distribution of lower-mass galaxies (Cappellari et al. 2013a). The deviation starts appearing around $M_\star \approx M_{\rm crit} \approx 2 \times 10^{11}$ M$_\odot$ and is particularly evident above $M_\star > 2 \times 10^{11}$ M$_\odot$. This deviation is the signature of multiple dry mergers expected to move galaxies along lines of nearly constant sigma (or $R_{\rm e} \propto M_\star$) on the ($M_\star$, $R_{\rm e}$) plane (e.g. C16).

Although there is some evidence for a possible change in the black hole–galaxy scaling relations with the currently existing $M_{\rm BH}$, it is not clear beyond the high-mass regime due to the limited number of measurements above $M_{\rm crit}$. Consider at (1) a given $\sigma_\star$ with $M_\star > M_{\rm crit}$ and (2) the range of measured $M_{\rm BH}$ (varying by more than ≈ an order of magnitude) and their uncertainties (a factor of ≈2), which depends strongly on the type of data and type of models used. The observation of this $M_{\rm BH}$ dependence transition from $\sigma_\star$ to $M_\star$ is difficult to see with the current data. Furthermore, this effect is hampered by the increasing closeness of constant-$\sigma_\star$ lines and the lack of galaxies with masses $M_\star > 10^{12}$ M$_\odot$. Our proposed sample of the most massive galaxies utilizes the unprecedented advantages

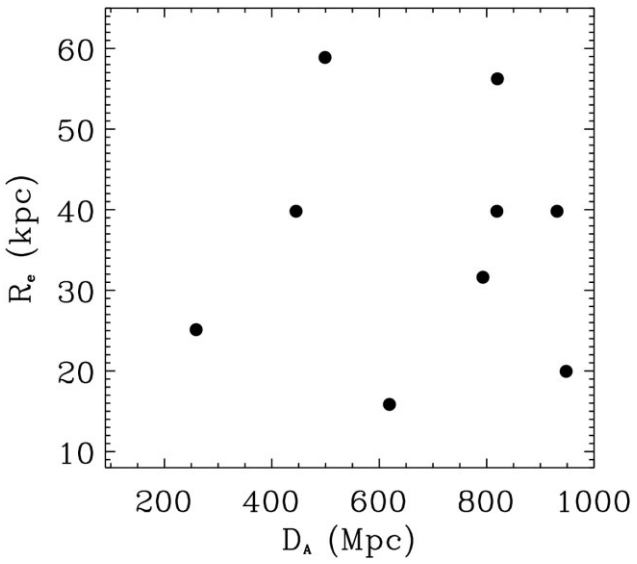

Figure 5. Nine galaxies in our MMBH sample span in the whole parameter space of angular-size distance and effective radius. Some specific properties of these nine galaxies are summarized in Tables 3 and 4. We perform HSIM IFS simulations for all nine ETGs.

of ELT/HARMONI IFS in both angular and spectral resolutions and sensitivity, aiming to resolve all of these difficulties and discover new physics in the previously untouchable regimes of SMBH and galaxy coevolution.

3.6 Nine representative targets for our MMBH survey

Our complete MMBH IFS survey sample of 101 ultramassive galaxies, shown by red dots in Figs 1 and 4, is not sensitive to the span of the galaxy stellar-mass parameter (see Table 2); thus the sample's properties are better examined in the D_A–R_e plane, because revealing the distributions of the SMBH (or MMBH) population as a function of redshift (D_A) and effective radii (R_e) of the hosts will shed light on the underlying physics that drive the central massive black holes and the host galaxies to obtain their masses and coevolution throughout cosmic time. To ensure that our ELT/HARMONI IFS simulations in subsequent sections (Sections 4, 5, and 6) represent the MMBH sample entirely, we select only nine targets from these 101 galaxies to perform HSIM to create IFS mock data cubes distributed over the full range of angular-size distance and size of our MMBH survey. Although these nine chosen targets are selected randomly from the D_A–R_e plane as shown in Fig. 5, they must cover the full parameter ranges of the galaxy's R_e and D_A. In this way, the reduced simulated sample minimally represents 101 ultramassive galaxies of the MMBH sample but optimally examines their SMBH/MMBH distributions at different cosmic times and galaxy densities.

3.7 Galaxy environments

As located at the highest galactic-mass ladder, galaxies in our MMBH-selected sample are commonly present in the centres of galaxy groups or clusters (Ma et al. 2014, C16). It is thus worth investigating the larger-scale environments where these $M_\star \gtrsim 2 \times 10^{12}\,M_\odot$ galaxies reside. Only one galaxy in our sample lies within the full-sky volumes ($D_A < 150$ Mpc) of two galaxy-group catalogues: 2MRS (Crook et al. 2007, 2008) and galaxy-redshift 2M+ + (Lavaux & Hudson 2011) but neither belong to these groups.

Dense galaxy clusters significantly impact the galaxy growth and the evolution of the black hole–galaxy scaling relations because of the material supply and mergers. However, isolated galaxies live in low-density environments, likely surrounded by faint satellite galaxies (Jones et al. 2003), and might have stopped building up their masses a few billion years ago. Thus, our MMBH survey will provide an excellent sample for studying environmental effects on galaxy formation (Mulchaey & Jeltema 2010).

Fig. 6 shows two-arcminute-squared field-of-view (FOV) SDSS red–green–blue images of the subsample of nine galaxies (Section 3.6) shown in Fig. 5 and listed in Tables 3, 4, and 5. Such a large FOV reveals the diverse intergalactic vicinity of these nine galaxies, ranging from isolated (e.g. 2MASXJ22354078+0129053, 2MASXJ12052321+1022461) with some small satellites to dense galaxy clusters (e.g. 2MASXJ00034964+0203594, 2MASXJ11480221+0237582). We also carefully examined other galaxies in the MMBH sample for available NGS and found at least one to three of them in their surrounding neighbourhood intergalactic environments, which satisfies our requirement (i.e. selection criterion iv), but show in Fig. 6 the representative subsample only. The requirement of an NGS will shrink our MMBH sample size further because only 80 per cent of the sample has such available NGS. As can be seen in Fig. 6, there are two galaxies in the reduced/simulated subsample (i.e. 2MASXJ12052321+1022461 and 2MASXJ11480221+0237582) that have no NGS, also showing that ≈80 per cent of the galaxies have NGS for LTAO performances.

4 DYNAMICAL AND PHOTOMETRIC MODEL

We first describe the dynamical model and the synthetic library of stellar spectra that we use in Sections 4.1 and 4.2, respectively. We next construct mass models of all nine chosen galaxies (see Fig. 5) for HARMONI IFS simulation in Section 4.3 (only showing the galaxy 2MASXJ12052321+1022461 as an example) whose properties cover and represent our MMBH survey as a whole.

4.1 Jeans anisotropic model (JAM)

Our sample of galaxies consists of the most massive galaxies. These are generally close to spherical or weakly triaxial in their central regions (C16). For this reason, we constructed mock kinematics using the dynamical model based on a solution of the Jeans equations, assuming axisymmetry with a spherical aligned orientation of the velocity ellipsoid, which is likely to provide a better approximation of the dynamics of slow rotators (Cappellari 2020, hereafter C20) as implemented in the JAM software (which we call the JAM_{sph} model).[4] To predict the mean velocity using JAM_{sph}, we assumed a model with a velocity ellipsoid axially symmetric around the radial direction, namely $\sigma_r \neq \sigma_\theta = \sigma_\phi$. This model converges to a non-rotating spherical model in the spherical limit and is an appropriate choice for modelling slow rotators expected to be not far from spherical in their central regions. This assumption corresponds to equation (55) of C20 achieved by setting `'gamma = beta'` in the `jam_axi_proj.py` procedure of JAM; see C20 for detailed descriptions of the model.

The details of the adopted model are not critical for this work, as here we are interested in estimating the formal errors in the M_{BH} determinations due to the effect of noise and spatial resolution rather

[4] JAMPY v6.4.0, available from https://pypi.org/project/jampy/

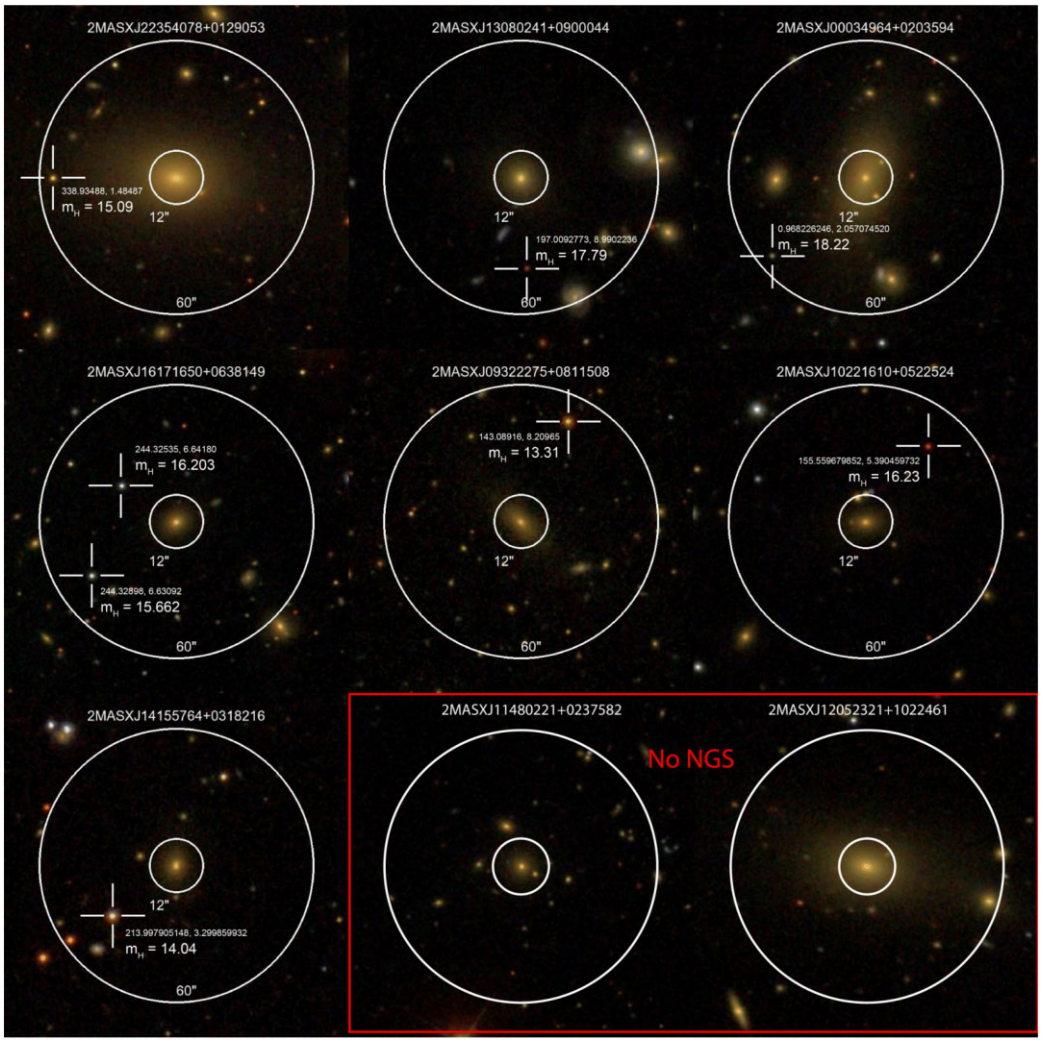

Figure 6. The red–green–blue SDSS images of the reduced subsample of nine galaxies for which we chose to perform HSIM IFS simulations shown in Fig. 5. The large FOV ($>2 \times 2$ arcmin^2) of these images reveals the intergalactic environments around these nine galaxies, ranging from isolated to dense galaxy clusters. The name of each galaxy is shown in the top corner, while the two white circles define the galaxy's allowable vicinity (12 arcsec $< r <$ 60 arcsec away from the galaxy centre) for the search for the faint NGS necessary for LTAO performance. The white crosses indicate the available NGS locations, showing their right ascension and declination in degrees and the apparent AB magnitudes measured in the *H* band. For two of the nine galaxies selected for our simulations in this work, we are unable to find NGS with our observational strategy, i.e. 2MASXJ12052321+1022461 and 2MASXJ11480221+0237582, shown in the red rectangle in the bottom right-hand corner.

Table 3. List of simulated targets and their core-Sérsic best-fitting parameters from *i*-band Pan-STARR images. The inner power-law slope is fixed with $\gamma = 0.1$.

Galaxy name	μ_b (mag arcsec^{-2})	n	α	r_b (arcsec)	R_e (arcsec)	μ_b (mag arcsec^{-2})	n	α	r_b (arcsec)	R_e (arcsec)
(1)	(2)	(3)	(4)	(5)	(6)	(7)	(8)	(9)	(10)	(11)
	MGE	MGE	MGE	MGE	MGE	IRAF	IRAF	IRAF	IRAF	IRAF
J22354078+0129053	15.34 ± 0.04	2.80 ± 0.03	2.98 ± 0.02	0.83 ± 0.02	5.03 ± 0.03	15.21 ± 0.03	2.52 ± 0.04	3.58 ± 0.03	0.98 ± 0.03	5.95 ± 0.03
J13080241+0900044	15.17 ± 0.03	2.97 ± 0.04	3.72 ± 0.04	0.79 ± 0.02	5.34 ± 0.04	15.14 ± 0.02	2.34 ± 0.02	3.75 ± 0.04	0.94 ± 0.02	6.04 ± 0.03
J12052321+1022461	15.36 ± 0.03	2.86 ± 0.05	2.79 ± 0.04	0.74 ± 0.05	5.40 ± 0.03	15.22 ± 0.04	2.43 ± 0.02	3.95 ± 0.01	0.95 ± 0.05	5.98 ± 0.04
J00034964+0203594	15.05 ± 0.04	2.92 ± 0.02	3.27 ± 0.03	0.81 ± 0.03	5.48 ± 0.05	14.97 ± 0.03	2.22 ± 0.03	3.89 ± 0.04	0.92 ± 0.04	6.12 ± 0.05
J16171650+0638149	15.30 ± 0.02	2.90 ± 0.02	3.85 ± 0.05	0.85 ± 0.04	5.52 ± 0.02	15.20 ± 0.05	2.21 ± 0.05	3.84 ± 0.05	0.91 ± 0.03	5.97 ± 0.05
J09322275+0811508	15.15 ± 0.05	2.88 ± 0.02	3.44 ± 0.03	0.90 ± 0.04	5.85 ± 0.05	15.16 ± 0.05	2.45 ± 0.03	3.69 ± 0.02	0.97 ± 0.02	5.83 ± 0.03
J10221610+0522524	15.13 ± 0.05	2.91 ± 0.03	3.81 ± 0.03	0.95 ± 0.03	5.57 ± 0.04	15.05 ± 0.06	2.26 ± 0.03	3.83 ± 0.01	0.95 ± 0.03	5.79 ± 0.05
J14155764+0318216	15.05 ± 0.05	2.90 ± 0.04	3.15 ± 0.02	0.93 ± 0.02	5.96 ± 0.03	14.93 ± 0.04	2.31 ± 0.05	3.52 ± 0.05	0.93 ± 0.03	5.82 ± 0.03
J11480221+0237582	15.31 ± 0.05	2.85 ± 0.03	3.60 ± 0.04	0.87 ± 0.02	5.82 ± 0.03	15.25 ± 0.05	2.57 ± 0.04	3.78 ± 0.01	0.97 ± 0.03	6.21 ± 0.05

Notes. Column 1: Galaxy name in which we assigned J ≡ 2MASXJ. The following five columns are the surface-brightness density μ_b at the break radius (column 2), the Sérsic index (column 3), the real galaxy profile parameter (column 4), the break radius (column 5), and the effective radius of the outer core-Sérsic profile (column 6) derived from the MGE 1D profile. The last five columns (7, 8, 9, 10, 11) are the same as the former five but derived from the IRAF `ellipse` 1D profile. Details of these five parameters of the core-Sérsic profile are given in the text (Section 4.3).

Table 4. List of simulated targets and their essential properties used for HSIM to produce their mock IFS simulated data cubes and kinematics.

Galaxy name	z	D_A (Mpc)	$\log R_e$ (kpc)	M/L_i ($M_\odot/L_\odot$)	$\sigma_\star$ (km s^{-1})	$M_\star$ (10^{12} $M_\odot$)	$M_{BH,\sigma_\star}$ (10^9 $M_\odot$)	$M_{BH,M_\star}$ (10^{10} $M_\odot$)	$R_{SOI,\sigma_\star}$ (arcsec)	$R_{SOI,M_\star}$ (arcsec)	NGS (arcsec, m_H)
(1)	(2)	(3)	(4)	(5)	(6)	(7)	(8)	(9)	(10)	(11)	(12)
J22354078+0129053	0.057 98	259	1.41	2.0	295	2.5	1.3	1.6	0.050	0.63	53, 15.09
J13080241+0900044	0.093 40	499	1.77	2.5	211	2.3	0.2	0.3	0.010	0.12	39, 17.79
J12052321+1022461	0.095 02	445	1.62	3.0	262	2.9	0.7	1.0	0.020	0.29	–, –
J00034964+0203594	0.118 12	420	1.75	2.0	243	4.0	0.5	0.9	0.018	0.32	53, 18.22
J16171650+0638149	0.153 57	619	1.23	3.0	405	2.5	6.6	8.2	0.057	0.72	43, 16.20
J09322275+0811508	0.192 51	793	1.50	2.5	272	2.6	0.8	1.0	0.015	0.12	48, 13.31
J10221610+0522524	0.255 31	819	1.61	2.5	232	2.5	0.4	0.4	0.008	0.08	43, 16.20
J14155764+0318216	0.302 12	931	1.63	3.0	320	4.4	2.0	4.0	0.019	0.37	35, 14.04
J11480221+0237582	0.313 99	948	1.33	2.5	346	3.0	3.0	4.4	0.025	0.35	–, –

Notes. Column 1: Galaxy name assigned to J ≡ 2MASXJ (Skrutskie et al. 2006). Column 2: galaxy's redshift (Huchra et al. 2012). Column 3: angular-size distance to the galaxy obtained from NED (double checked with https://www.astro.ucla.edu/~wright/CosmoCalc.html and redshift; Wright 2006, gives a slightly different in angular-size distance, probably because of the unclear indication of either D_A or D_L in NED). Column 4: galaxy's effective radius (or half-light radius $R_e = 1.61 \times j\_r\_eff$; Skrutskie et al. 2006; Cappellari 2013; Cappellari et al. 2013a, K18). Column 5: assumed mass-to-light ratio (estimated in Section 5.2). Column 6: stellar velocity dispersion from the galactic bulge component $\sigma_\star^2 = G \times M_\star/(5 \times R_e)$ (K18). Column 7: the galaxy's stellar mass (equation 2 of Cappellari et al. 2013a, $\log(M_\star) = -0.44 \times (M_K + 23) + 10.58$). Column 8: central SMBH mass estimated based on equation (2) from K18. Column 9: central MMBH mass estimated based on equation (3) from K18. Column 10: R_{SOI} of SMBH calculated from $\sigma_\star$ and central SMBH mass estimated based on equation (2) from K18. Column 11: R_{SOI} of MMBH calculated from $\sigma_\star$ and central MMBH mass estimated based on equation (3) from K18. We calculate these two R_{SOI} using equation (1). Column 12: Natural guide star distance from the galaxy centre and its apparent H-band magnitude used in the LTAO mode for the atmospheric turbulence correction.

Table 5. Mock HSIM IFS of the nine chosen targets (DIT = 900 s = 15 min).

Galaxy name	HSIM band	Exp. time DIT × NDIT (min)	Sensitivity – (min)
(1)	(2)	(3)	(4)
J22354078+0129053	$I_z, H+K$	30 = DIT × 2	10
J13080241+0900044	$I_z, H+K$	45 = DIT × 3	15
J12052321+1022461	$I_z, H+K$	45 = DIT × 3	15
J00034964+0203594	$I_z, H+K$	60 = DIT × 4	15
J16171650+0638149	$I_z+J, H+K$	60 = DIT × 4	15
J09322275+0811508	$I_z+J, H+K$	75 = DIT × 5	20
J10221610+0522524	$I_z+J, H+K$	90 = DIT × 6	30
J14155764+0318216	$I_z+J, H+K$	120 = DIT × 8	45
J11480221+0237582	$I_z+J, H+K$	120 = DIT × 8	45

Notes. Column 1: Galaxy name assigned to J ≡ 2MASXJ (Skrutskie et al. 2006). Column 2: HSIM band chosen to perform IFS simulation for observational mock data cubes and their kinematic measurements. The choice of these HSIM bands is optimal and is a trade-off between redshift and spectral resolution. Column 3: real exposure time entered into HSIM for our simulated kinematics maps presented in Figs 10 and 11 and Figs A1, A5, A9, A13, A17, A21, A25, A29 in Appendix A. Column 4: Sensitivity in terms of exposure time at which we test the lowest limit of S/N from the simulated IFS so that our PPXF still extracts accurate kinematics (will be discussed later in Section 6.2). We should note that the estimated times shown in Columns 3 and 4 are the science times on target without accounting for the target acquisition, overhead, and AO setup time.

than the possible systematic biases of the modelling methods. We plan to study the latter in the future.

4.2 MARCS synthetic library of stellar spectra

We utilized the library of stellar population synthesis (SPS) spectra[5] by Maraston & Strömbäck (2011), based on the MARCS synthetic library of theoretical spectra by Gustafsson et al. (2008). Although MARCS synthetic library spectra are not as reliable as an empirical stellar library, they have broad wavelength coverage (i.e. the vacuum wavelength covers from 1300 Å to 20 μm) and high spectral resolution ($\sigma = 6.4$ km s^{-1} or $R = \lambda/\Delta\lambda = 20\,000$), sampling with 100 724 flux points ($\Delta\lambda \approx 0.065$ Å). We also assumed the Salpeter IMF, 10 Gyr, and Solar metallicity (z002) and truncated the SPS within the wavelength coverage of 0.7–2.5 μm for the HARMONI/I_z, $I_z + J$, and $H + K$ gratings.

4.3 Galaxy mass models

4.3.1 The need for high-resolution imaging

In order to obtain accurate constraints from dynamical modellings (e.g. M_{BH} and galaxy kinematics), the galaxy-mass model must be precisely constructed at all components (i.e. stellar remnants, stars, dust, gas, dark matter) and scales (i.e. from a few tens of parsecs away the galaxy centre, where it is comparable to or within r_{SOI}, to hundreds of kiloparsecs at the dark matter halo). Thus, wide-field images from broad-band photometries at the same spatial resolutions (20–100 mas) and wavelength coverages (0.7–2.47 μm) of HARMONI IFS are highly demanded. In some cases, optical images (0.45–0.76 μm) are also necessary to examine the galaxy's stellar variations and gas/dust extinction. Currently, such high-angular-resolution images for our MMBH IFS survey do not exist in any archival data bases except for their low-resolution ground-based images in optical and NIR surveys (e.g. Pan-STARRS, SDSS, 2MASS), which lack critical information on matter distribution at the scale of a few times r_{SOI}. Using these available images without some appropriate assumptions to extrapolate the stellar distribution toward the galaxy centre will bias the M_{BH} estimate.

Imaging from space missions such as *HST* or *JWST* are possible alternatives as they probe deeper into the central regions, a few times the MMBH's r_{SOI} (≈50–100 mas), helping to reduce uncertainty on the M_{BH} estimate significantly. To obtain accurate measurements of the motions of stars (and gas) within r_{SOI} – the key for reliable M_{BH} estimates – a telescope must be able to at least marginally resolve it. Currently, the Enhanced Resolution Imager and Spectrograph (ERIS)

[5]Available from https://marcs.astro.uu.se/

on VLT provides the highest available spatial resolution (≈50 mas), but even this is too low to probe the SOI of a typical SMBH beyond 100 Mpc, while our MMBH is detectable only out to $D_A \approx 200$ Mpc (see Fig. 1).

Ideally, possibly native ELT imaging obtained from the Multi-AO Imaging Camera for Deep Observations (MICADO) imager (FOV: 50.5 × 50.5 arcsec, wavelength: 0.8–2.4 μm, filters: *IYJHK* broad-band) at the same angular resolution (FWHM$_{PSF} \approx 10$ mas; Davies et al. 2010) with HARMONI is the best choice. MICADO takes advantage of the wide-field correction and uniform PSF offered by the multiconjugate AO (MCAO) module to achieve almost a full arcminute-squared FOV with 4 mas pixels to sample the diffraction limit, then fully resolves the MMBH's r_{SOI} to a few hundred Schwarzschild radii ($r_g = 2GM_{BH}/c^2 \approx 0.001$–400 au for black holes with masses in the range of 10^5–10^{10} $M_\odot$; 1 au is the Sun–Earth distance = 150 000 000 km), thus providing excellent opportunities to observe the purely Keplerian motion of stars caused mainly by the central black hole's gravitational potential. Thus, the combination of HARMONI IFS and the MICADO imager of ELT will be able to detect 10^4 $M_\odot$ black holes at distances of $D < 10$ Mpc (Nguyen et al., in preparation); heavier black holes ($M_{BH} \approx 10^9$ $M_\odot$), will be detected up to distances of $D_A \approx 1$ Gpc ($z \approx 0.3$; this work).

4.3.2 *Building and extrapolating the galaxy-mass models*

In this work, we used ground-based images and extrapolated the surface-brightness profiles following some assumptions sufficient for presenting the simulations and dynamical models. Among various ground-based images available (e.g. SDSS, Pan-STARRS, and 2MASS), Jensen et al. (2021) found the original Data Releases 1 (DR1) cutout images of Pan-STARRS are best even with their cosmetic defects for measuring large galaxies. In addition, the 2MASS, *HST*/Advanced Camera for Surveys (ACS), Pan-STARRS, and SDSS photometric magnitude systems are consistent near the centres of the galaxies. However, the Pan-STARRS profiles remain the same with ACS farther out, while the SDSS and 2MASS are not as deep, and the surface-brightness measurements become inconsistent and noisy in the outer portion of the galaxy. We repeated this test carefully for nine chosen galaxies for the HARMONI IFS simulation listed in Table 3 using both SDSS and Pan-STARRS images and found our conclusion to be consistent with that of Jensen et al. (2021). We therefore adopted the Pan-STARRS images for our photometric calibration. We thus performed the Pan-STARRS flux calibration to convert the imaging unit from counts s^{-1} to surface brightness in each pixel following the prescription described in section 3.2 of Jensen et al. (2015). Note that the full-sky images and the cutout images do not have identical photometric calibration to that mentioned on the Pan-STARRS1 (PS1, including DR1 and DR2) Image Cutout Service webpage.[6] The cutout images are combined from several input images and divided by the imaging keyword `EXPTIME`. These images' individual photometric `ZERO POINTS` are in the imaging header, but we used the median value.

We adopt the multi-Gaussian expansion method (MGE; Emsellem, Monnet & Bacon 1994; Cappellari 2002) to describe the galaxy surface brightness observed with Pan-STARRS/*i* band (i.e. cutout images obtained via PS1;[7] Chambers et al. 2016) with the algorithm and software[8] of Cappellari (2002). During the fit, the model convolves (or analytically deconvolves the Pan-STARRS image) with an adopted *i*-band Gaussian PSF with a median full width at half-maximum of FWHM ≈ 1.25 arcsec (Magnier et al. 2020; Waters et al. 2020).

We show the Pan-STARRS/*i*-band image and the best-fitting MGE model for the galaxy 2MASXJ12052321+1022461 in Figs 7 and 8 as an example, illustrating the agreement/disagreement between the data and the model in the forms of radial profiles and 2D contours at the same radii and contour levels, respectively.

However, in this work, we did not use the above best-fitting MGE models of the Pan-STARRS/*i*-band images directly in our kinematic models because of their low angular resolutions and coarse pixel

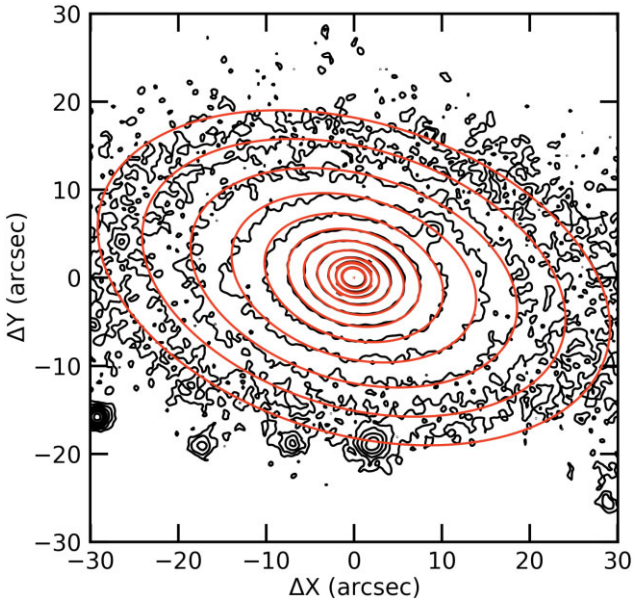

Figure 7. Comparison between the Pan-STARRS/*i*-band image photometric data (black) versus the best-fitting MGE model (red) of the galaxy 2MASXJ12052321+1022461 at the same radii illustrated in the form of 2D surface-brightness density contours in the FOV of 60 × 60 arcsec. Contours are spaced by 0.5 mag arcsec^{-2}.

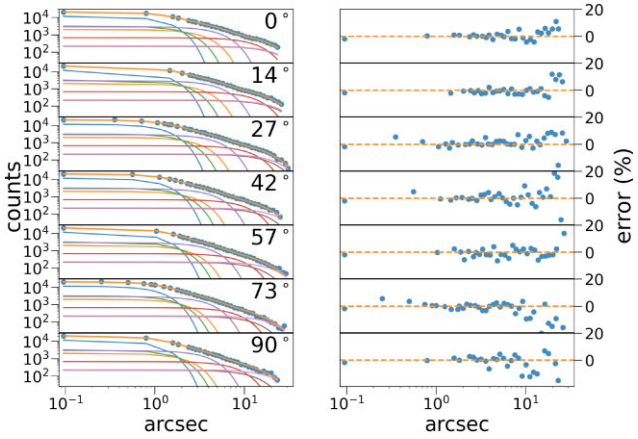

Figure 8. Same as Fig. 7, showing a comparison between the Pan-STARRS/*i*-band image photometry of 2MASXJ12052321+1022461 (blue dots) and its corresponding best-fitting MGE model with seven Gaussians at different position angles (colour lines, left-hand panels) within the FOV of 60 × 60 arcsec, along with the correspondingly fractional errors `(data---model)/data` in the right-hand panels.

[6] https://panstarrs.stsci.edu/
[7] http://ps1images.stsci.edu/cgi-bin/ps1cutouts
[8] v5.0.14, available from https://pypi.org/project/mgefit/

sampling (1 pixel $\approx$ 0.25 arcsec) compared to the desired scales of HARMONI in our simulations (pixel sampling of 10 mas). We used them to constrain the outer surface-brightness profiles of our chosen simulated galaxies, then extrapolated these profiles towards the regime of 10 mas surrounding their central black holes. We used the Trujillo et al. (2004) core-Sérsic profile (Sersic 1968) because our most massive galaxy sample comprises core galaxies:

$$I(r) = I' \left[1 + \left(\frac{r_b}{r}\right)^{\alpha}\right]^{\frac{\gamma}{\alpha}} \exp\left\{-b\left[\frac{(r^{\alpha} + r_b^{\alpha})}{r_e^{\alpha}}\right]^{\frac{1}{n\alpha}}\right\}, \quad (3)$$

where $I' = I_b 2^{-\frac{\gamma}{\alpha}} \exp\left[b 2^{\frac{1}{n\alpha}} \left(\frac{r_b}{r_e}\right)^{\frac{1}{n}}\right]$ and b is a function of the various parameters (n, α, γ, r_b, and r_e) that can be determined by solving the relation (A10) of Trujillo et al. (2004) when the enclosed luminosity at r_e is equal to half of the total luminosity, $2L(r_e) = L_T$. In numerical practice, Ciotti & Bertin (1999) use the asymptotic expansion theorem for the $1/r^n$ law to solve for b as an analytical function of the Sérsic index n as $b = 2n - \frac{1}{3} + \frac{4}{405n} + \frac{46}{25515n^2} + O(\frac{1}{n^3})$. Here, n is the Sérsic index, which controls the shape of the outer Sérsic part. r_e is the effective radius of the profile. r_b is the break radius, which is the point at which the surface brightness changes from the outer Sérsic part to the inner power-law regime of the profile. I_b is the intensity at the break radius (converted to surface-brightness density μ_b in Table 3) that controls the sharpness of the transition between the cusp and the outer Sérsic profile. α is the sharpness parameter, which describes the transition between the outer Sérsic and inner power-law regimes.

First, we converted the best-fitting deconvolved MGE models into one-dimensional (1D) surface-brightness profiles, then fitted them with the core-Sérsic function above. Here, we fixed the inner power-law slopes of the core-Sérsic profiles with the typical $\gamma = 0.1$ for core galaxies (e.g. Lauer et al. 2007b) expected in the brightest galaxies (e.g. Faber et al. 1997), while allowing the other five parameters to vary. Table 3 shows the best-fitting values of these five free parameters of the surface-brightness profiles of the nine chosen simulated galaxies.

As a sanity check, we used the Image Reduction and Analysis Facility (IRAF) `ellipse` task (Jedrzejewski 1987) to extract radial surface-brightness profiles of the stars in concentric annuli with varying position angles and ellipticities, although keeping both fixed does not change our results (Nguyen et al. 2022). We then fitted these stellar radial light surface-brightness profiles with a core-Sérsic function. The fits were carried out using a non-linear least-squares algorithm (IDL MPFIT function;[9] Markwardt 2009). To compare the model and data, before extracting the 1D spatially deconvolved (i.e. intrinsic) IRAF profile, we first made a two-dimensional (2D) Gaussian PSF adopted from the Pan-STARRS *i*-band image above, and secondly convolved it with the image. Thirdly, we iterated the core-Sérsic function to the spatially deconvolved profile for its best-fitting parameters. We show the consistency of these two approaches in determining the best-fitting parameters of the core-Sérsic profiles using the case of the galaxy 2MASXJ12052321+1022461 in Fig. 9 as an example and list these parameters for all nine simulated galaxies in Table 3.

Secondly, we used these derived parameters to reconstruct the interpolated MGE model towards the central 10 mas for each galaxy

[9]Available from http://purl.com/net/mpfit.

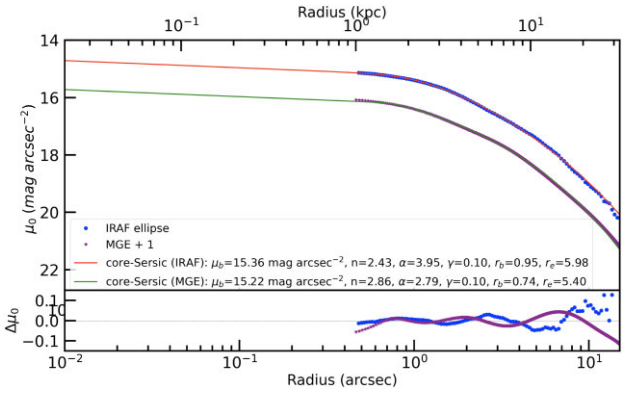

Figure 9. Upper panel: An example of the Pan-STARRS/*i*-band surface-brightness profiles of the galaxy 2MASXJ12052321+1022461 constructed either directly from IRAF `ellipse` (blue dots) or indirectly from the MGE model (purple stars). All magnitudes are corrected for foreground extinction. For clarity, we shifted the MGE surface-brightness profile by +1 mag. The best-fitting core-Sérsic surface-brightness profiles of these IRAF `ellipse` or MGE models are plotted in solid red and blue, respectively, and their best-fitting parameters are shown in the legend. We should note that within the radius of 0.8 arcsec of these 1D profiles, we fixed $\gamma = 0.1$ (see text in Section 4.3 for details) and did not fit these parts to the data. Lower panel: The differences, or residuals (`data---model`), between the IRAF `ellipse` (blue dots) and MGE (purple stars) surface-brightness profiles and their corresponding best-fitting core-Sérsic models illustrate the fit's goodness.

via the `mge_fit_1d.py` routine (Cappellari 2002, see footnote 9) to fit the analytic core-Sérsic with a constant ellipticity $\epsilon = 0$ and 10 Gaussians across radii of $\approx$14 to $\approx$30 arcsec, depending on the apparent size of the galaxies.

Finally, we created a mass-follow-lightsurface density by assuming a constant M/L_i. This stellar-mass component will be added to an SMBH or an MMBH with a specific mass as a point source. In this work, we ignored (1) the possible variation in M/L inferred from stellar population variation (McConnell et al. 2013; Li et al. 2017; Mitzkus, Cappellari & Walcher 2017; Nguyen et al. 2017, 2018, 2019; Nguyen et al. 2020, 2021, 2022) as we concern ourselves with the stellar kinematics within the FOV of 0.4 $\times$ 0.4 arcsec of HARMONI only where the central black hole's potential dominates. In this nuclear region, any possible M/L gradient due to the stellar population or dark matter is insignificant for our tests.

5 HARMONI IFS SIMULATION

We first describe the HARMONI instrument on ELT and the HSIM simulator in Section 5.1. Next, we combine the mass-MGE models of all nine chosen galaxies constructed in Section 4.3 with the HSIM simulator to simulate their I_z (0.83–1.05 μm), $I_z + J$ (0.81–1.37 μm), and $H + K$ (1.45–2.45 μm) mock data cubes in Section 5.2. Finally, we present the extracted kinematics of all nine galaxies with different redshifts and sizes (also known as D_A versus R_e, Fig. 5) in Section 5.3.

5.1 HARMONI instrument and HSIM simulator

HARMONI is an optical and NIR instrument on ELT, which will provide IFS at four different spatial scales (i.e. 4 $\times$ 4, 10 $\times$ 10, 20 $\times$ 20, and 30 $\times$ 60 mas^2) and three spectral resolving powers (i.e. $\lambda/\Delta\lambda \approx$ 3355, $\approx$ 7104, and $\approx$ 17 385). Given a 39 m single field in design with 798 hexagonal segments (each $\approx$1.4 m across), ELT can collect spectra of 152 $\times$ 214 ($\approx$32 530) spaxels equipped with

laser guide star AO. This technical design is best to perform a wide range of science programs from diffraction-limited to ultrasensitive ones such as morphology, spatially resolved populations and kinematics, abundances, and line ratios of distant sources (Thatte et al. 2016), allowing it to achieve a particular S/N in a relatively short exposure time, even in faint surface-brightness targets. In particular, such unprecedentedly powerful techniques will revolutionize our understanding of the physics of mass assembly in high-redshift galaxies and our search for the missing intermediate-mass black hole (IMBH, $M_{\rm BH} \lesssim 10^5$ M$_\odot$) population in nearby dwarf galaxies or stellar clusters (Zieleniewski et al. 2015; García-Lorenzo et al. 2019). A full description of the instrument is presented in Thatte et al. (2020) and on the HARMONI webpage.[10]

HARMONI Simulator (HSIM[11]) is the pipeline for simulating observations with the HARMONI instrument on ELT (Zieleniewski et al. 2015). It uses high-spectral- and spatial-resolution IFS cubes without random noise generated in Section 5.2 as inputs, encodes with the celestial target's physical properties, and then creates simulated cubes. The simulations incorporate detailed models of the atmospheric effects and realistic detector statistics to mimic realistic mock data. This paper concentrates in depth on the simulations of the ELT AO observations' quality by measuring the nuclear-stellar kinematics in distant galaxies and estimating their $M_{\rm BH}$. From those, we will explore the limits at which HARMONI can produce feasible observables.

5.2 Simulations of the mock IFS data cubes

To understand the effects of high redshift and galaxy size on the stellar kinematic measurements and sensitivities, we chose to simulate the HARMONI IFS observations in nine galaxies with different redshifts and sizes using the dedicated HSIM pipeline (see footnote 11). Due to our survey's wide range of redshifts ($0.028 < z \lesssim 0.3$), specific stellar features are used to estimate the nuclear-stellar kinematics shift along the spectral dimension differently for each target. The CO-bandheads absorptions (2.29–2.47 μm; e.g. CO(2–0) λ2.293 μm and CO(3–1) λ2.312 μm bands) fall off the $H+K$ and K bands and cannot be used for galaxies with $z > 0.04$. Nevertheless, the CaT stellar absorption (0.86–0.88 μm) features stay safely within the I_z band for galaxies with $z < 0.12$ and within the $I_z + J$ band for our other selected galaxies with higher redshift. Additionally, to account for the spectral resolutions and to test the feasibility of different stellar features, we performed simulations for the I_z band (0.83–1.05 μm) and $I_z + J$ band (0.81–1.37 μm), which have $\sigma_{\rm instr} \approx 18\,{\rm km\,s^{-1}}$, $\lambda/\Delta\lambda \approx 7104$ and $\sigma_{\rm instr} \approx 38\,{\rm km\,s^{-1}}$, $\lambda/\Delta\lambda \approx 3355$, respectively. It is also necessary to test the capacity of using some stellar features in the $H+K$ band (1.45–2.45 μm) to measure the stellar kinematics, which are not used widely in the current works (but see Crespo Gómez et al. 2021).

Depending on redshift, some strong absorption lines from atomic species at the blue part of the K band shifted to its red part (e.g. Na I λ2.207 μm, Ca I λ2.263 μm, and Mg I λ2.282 μm) for $z < 0.1$ galaxies in the MMBH sample. Also, a larger number of atomic absorption lines in the H band (e.g. Mg I $\lambda\lambda$1.487, 1.503, 1.575, 1.711 μm, Fe I λ1.583 μm, and Si I λ1.589 μm) remain on the $H+K$ band for the remaining higher-redshift galaxies. In addition, there are several strong CO absorption features that are very sensitive to the star surface gravity and effective temperature in the H band (Silge & Gebhardt 2003; Crespo Gómez et al. 2021) mainly produced in the atmospheres of evolved giant stars, with a non-negligible contribution of cool asymptotic giant branch (AGB) stars (Kleinmann & Hall 1986; Dallier, Boisson & Joly 1996; Wallace & Hinkle 1997; Förster Schreiber 2000; Böker et al. 2008; Kotilainen et al. 2012; Dametto et al. 2014) such as CO(3–0) λ1.540 μm, CO(4–1) λ1.561 μm, CO(5–2) λ1.577 μm, CO(6–3) λ1.602 μm, CO(7–4) λ1.622 μm, and CO(8–5) λ1.641 μm (see Fig. 11). We relied on these atomic absorption lines and CO absorption features as the most significant carriers of the kinematic information – whenever they are on the redshifted wavelength coverages of the $H+K$ grating – to build the inputs and to extract stellar kinematics from the outputs of HSIM in this work. They will be the benchmark for future usage in deriving stellar kinematics from IFS data.

All essential properties of the nine chosen galaxies needed for the modellings are presented in Table 4, while the chosen grating IFS and HSIM simulations are shown in Table 5. However, regarding the AO performance during HSIM simulations, we did not use the appropriate NGS listed in Table 4 for each galaxy (i.e. we cannot find a realistic NGS for two galaxies in this simulated sample) but supplied these simulations with the LTAO mode with a star of 17.5 mag in the H band within a distance of 30 arcsec, the standard zenith seeing of FWHM = 0.64 arcsec, and an airmass of 1.3. These parameters are defaulted in HSIM to perform median observational conditions but can be changed from target to target as long as the selected criterion (iv) mentioned in Section 2.2 is satisfied. The necessary NGS information listed in Column 10 of Table 4 and shown in Fig. 6 is a reduced version of 101 selected galaxies, showing the robustness of LTAO performances for our MMBH IFS survey. The LTAO mode combines six off-axis LGS with a faint NGS to deliver diffraction-limited image quality over a large fraction of the sky. It also implements several off-axis wavefront sensors, but optimizes them to analyse the centre while better sampling the on-axis turbulence cylinder of the FOV in detail, resulting in high performance across a small FOV, limited by tomographic error, low-order residuals, and increased (medium) sky coverage.

We simulated the IFS within the FOV of 400 × 400 mas^2 and sampled the pixel size to 10 × 10 mas^2. This choice of a 10 mas pixel size ensures that we sample the ELT PSF FWHM of 12–18 mas with 1–2 spaxels (Thatte et al. 2016, 2020), resulting in precise kinematic measurements at the galaxy centre on the scale of a factor 2 × smaller than the resolving power in radius (i.e. our given proposed survey spatial resolution of 20 × 20 mas^2 gives ≈12 pixels within the black hole SOI with the simulated pixel sampling of 10 × 10 mas^2). Thus, the stellar kinematics dominated mainly by central black holes will be robustly detected. The exposure time of each simulation will change substantially depending on redshifts and gratings to ensure an S/N in every spaxel at the measured stellar features $\gtrsim$5, but we will bin pixels together later for higher S/N. However, to mimic the actual observations on ELT, we applied multi-exposure frames and dithering by setting `DIT` = 900 s (15 min) for each; the total exposure time will be counted by the number of exposures `NDIT` = `an integer` in the HSIM pipeline.

For simplicity, we assumed the light-of-sight velocity distribution (LOSVD) to be Gaussian (e.g. $V_{\rm rms}^2 = V^2 + \sigma_\star^2$). Thus, we created the 2D intrinsic first and second velocity moments (i.e. V and $\sigma_\star$) in terms of a Gaussian using the JAM$_{\rm sph}$ modelling (C20) and the galaxy-mass model mentioned in Sections 4.1 and 4.3, respectively.

We also assumed a constant M/L_i (Table 4) to convert the axisymmetric stellar-light MGEs inferred from the core-Sérsic profile (Table 3) into the galaxy-mass model for each galaxy. This M/L_i was estimated using the Pan-STARRS ($g-i$) colour and the Roediger et al. (2015) colour–M/L scaling relation assuming the Charlot & Fall

[10] http://harmoni-web.physics.ox.ac.uk/

[11] v3.10, available from https://github.com/HARMONI-ELT/HSIM

(2000) prescription for dust + interstellar medium (ISM) attenuation correction. Details of these colour–M/L conversion and dust + ISM correction processes followed the descriptions by Nguyen et al. (2018). In order to estimate the M/L_i accurately, we calculated the background level of each image in small regions as far away from the galaxy centre as possible (radial range of 20–35 arcsec depending on the apparent size of each galaxy) and subtracted it. The 5×5 arcsec central regions of these nine chosen simulated galaxies show mostly constant $(g - i)$ colour for each nucleus with values ranging from 1.17–1.35 mag, resulting in constant M/L_i changes from 2.0 ($M_\odot/L_\odot$) to 3.0 ($M_\odot/L_\odot$) (see fig. 7 and table 1 of Roediger et al. 2015 for estimating the M/L-based colour).

In the JAM$_{\rm sph}$ modellings (C20), we assumed an average inclination ($i \approx 60^\circ$) and chose to model three kinematics of three different $M_{\rm BH}$, including $M_{\rm BH} = 0$ M$_\odot$ and two other black holes, either (i) following the $M_{\rm BH}$–$\sigma_\star$ relation or (ii) assuming that $M_{\rm BH}$ follows $M_{\rm BH}$–$\sigma_\star$ for $M_\star < M_{\rm crit}$ and switches to being proportional to $M_\star$ for $M_\star > M_{\rm crit}$. For this, we used equations (2) and (3) of K18, respectively. These two black hole masses for each simulated galaxy are presented in Table 4. The kinematic maps were computed with JAM$_{\rm sph}$ on a regular grid with an FOV of 200×200 mas^2 and a pixel size of 5×5 mas^2. This scale will be convolved with the HARMONI PSF, rebinned, and interpolated to the specific pixel-sampling scale of 10×10 mas^2 by HSIM. Also, previous dynamical analysis with the IFS (e.g. WHT/OASIS and VLT/SINFONI) and the Schwarzschild orbit-based model (Schwarzschild 1979) that included the effects of a central SMBH, the mass distribution of the stars, and a dark matter halo for massive (core) slow-rotator galaxies found the tangential anisotropy ($\beta_r < 0$) in the cores and radial anisotropy ($\beta_r > 0$) at larger radii among the population of stellar orbits (Cappellari et al. 2008; Thomas et al. 2014). We thus accounted for this fact in our simulations by adopting $\beta_r = -0.2$ for several innermost MGE components inferred mainly from the power-law part, which describes the core of the surface-brightness profile separated from the outer Sérsic one by the break radius $r_{\rm b}$, and $\beta_r = +0.2$ for the rest, while setting the tangential anisotropy of the individual kinematic-tracer MGE Gaussians, $\sigma_\theta = \sigma_\phi$, as assumed in equation (55) of C20.

Given all those assumptions, we created an input noiseless-IFS cube for HSIM by employing the following steps:

(i) We accounted for the targets' redshifts on the MARCS SPS spectra by shifting the spectral range (i.e. for specific HARMONI grating bands) by a factor of $(1 + z)$.

(ii) We logarithmically rebinned the synthetic stellar spectrum of the chosen population (SPS; Section 4.2) to a scale at which the velocity scale is set as `velscale` $= 2\,{\rm km\,s^{-1}}$ so that the spectrum has constant $\Delta \log \lambda$ intervals.

(iii) For each spatial position in the cube, we constructed the kinematics `Gaussian kernel`, sampled at steps $\Delta V = 2\,{\rm km\,s^{-1}}$, with the mean velocity and velocity dispersion $(V, \sigma_\star)$ computed by the JAM$_{\rm sph}$ model for that position.

(iv) We convolved the logarithmically rebinned spectrum created from step one with the `Gaussian kernel` generated from step two, then linearly interpolated this logarithmically rebinned spectrum to the constant wavelength step $\Delta\lambda \approx 0.02$ Å, which is small enough so that no information is lost by the interpolation.

(v) We rebinned the spectrum by coadding an integer number of adjacent spectral pixels to reach a step in wavelength at a minimum $2\times$ smaller than the smallest HARMONI instrumental resolution in terms of FWHM (e.g. for the *JHK* gratings, $\Delta\lambda \approx 0.2$ nm $= 2$ Å). This is a rigorous integral over the pixels, and no information is lost.

(vi) We stored the resulting redshifted linearly sampled LOSVD-convolved noiseless spectrum in a cube.

(vii) We estimated the surface brightness of each galaxy (i.e. integrated intensities) using its core-Sérsic MGE model inferred from Table 3, then assigned every spaxel's intensity to its corresponding linearly sampled LOSVD-convolved noiseless spectrum in the cube. Since the core-Sérsic profile only describes the galaxy's surface brightness along the major axis, our galaxies are not all spherical. To deal with the galaxy shapes, we computed the elliptical radius of every pixel using the relation $r_{\rm ellipse} = \sqrt{x^2 + \left(\frac{y}{q}\right)^2}$, where x, y, and q are the positions of pixels (x, y) and the axis ratio from the stellar-light MGE model (Section 4.3), respectively, then assigned the flux by the core-Sérsic profile $I(r_{\rm ellipse})$ in equation (3).

(viii) We scaled the template spectrum in each 5×5 mas^2 spaxel in such a way that its mean flux in the i band, in erg s^{-1} cm^{-2} Å^{-1}, is equal to the surface brightness, in erg s^{-1} cm^{-2} Å^{-1} arcsec^{-2}, times the 5×5 mas^2 spaxels area. The robustness of our surface-brightness estimations is critical to the HARMONI sensitivity (and thus the required S/N within a reasonable exposure time), and should be high enough for measuring the stellar (or ionized gas emission, if detected) kinematics accurately. In Section 4.3, we tested the consistency of the surface brightness derived from the Pan-STARRS and SDSS images at the galaxy centres.

5.3 HSIM mock data cubes and extracted kinematics

Figs 10 and 11 show kinematic maps of the galaxy 2MASXJ11480221+0237582, the furthest target in our simulated sample ($z \approx 0.3$) as an example, extracted from the $I_z + J$ and $H + K$ HSIM mock data cubes with the JAM$_{\rm sph}$ model (C20), respectively. In each figure, three different black holes that have different masses are assumed to reside at the galaxy centre, including zero black holes ($M_{\rm BH} = 0$ M$_\odot$), $M_{{\rm BH},\sigma_\star} = 3 \times 10^9$ M$_\odot$ (equation 2 of K18), and $M_{{\rm BH},M_\star} = 4.4 \times 10^{10}$ M$_\odot$ (equation 3 of K18), are shown in each row (see also Table 4).

In order to create these maps, we adopt the adaptive Voronoi binning method (VORBIN;[12] Cappellari & Copin 2003) to spatially bin 2D data to the threshold-adopted S/N $\gtrsim 75$ per bin. This technique increases the S/N by adding up the signals of many spaxels within one bin and reduces the uncertainty of the kinematic measurement of that bin. We also took into account both the quality of the simulated data and the quality of the spectral fit by using the signal-to-residual-noise ratio (S/rN) measured as the standard deviation of the residuals between the galaxy spectrum and the best-fitting Penalized PiXel-Fitting (PPXF;[13] Cappellari 2022) model to define a residual noise (rN) for each Voronoi bin. Due to the high S/rN of the mock data cubes as seen in the left-hand panels of these figures, we obtained a small root-mean-squared velocity scatter with typical values of $\Delta V_{\rm rms} \lesssim 2.5$ per cent (i.e. $\Delta\sigma_\star \lesssim 2$ per cent and $\Delta V \lesssim 1$ per cent). In the successive panels of each row plot, the kinematic maps show an order with rotation subtracted for the systemic $V_{\rm sys}$, velocity dispersion $\sigma_\star$, and root-mean-squared velocity $V_{\rm rms} = \sqrt{V^2 + \sigma_\star^2}$.

We also demonstrate in these figures the PPXF fits for these kinematic maps using the stellar CaT-absorption features (1.06–1.14 μm) in the $I_z + J$ band and some strongly stellar features (e.g. 1.95–2.15 μm) in the $H + K$ band for 2MASXJ11480221+0237582 at the redshift $z \approx 0.3$. During this PPXF fit between the mock simulated

[12] v3.1.5, available from https://pypi.org/project/vorbin/
[13] v8.2.1, available from https://pypi.org/project/ppxf/

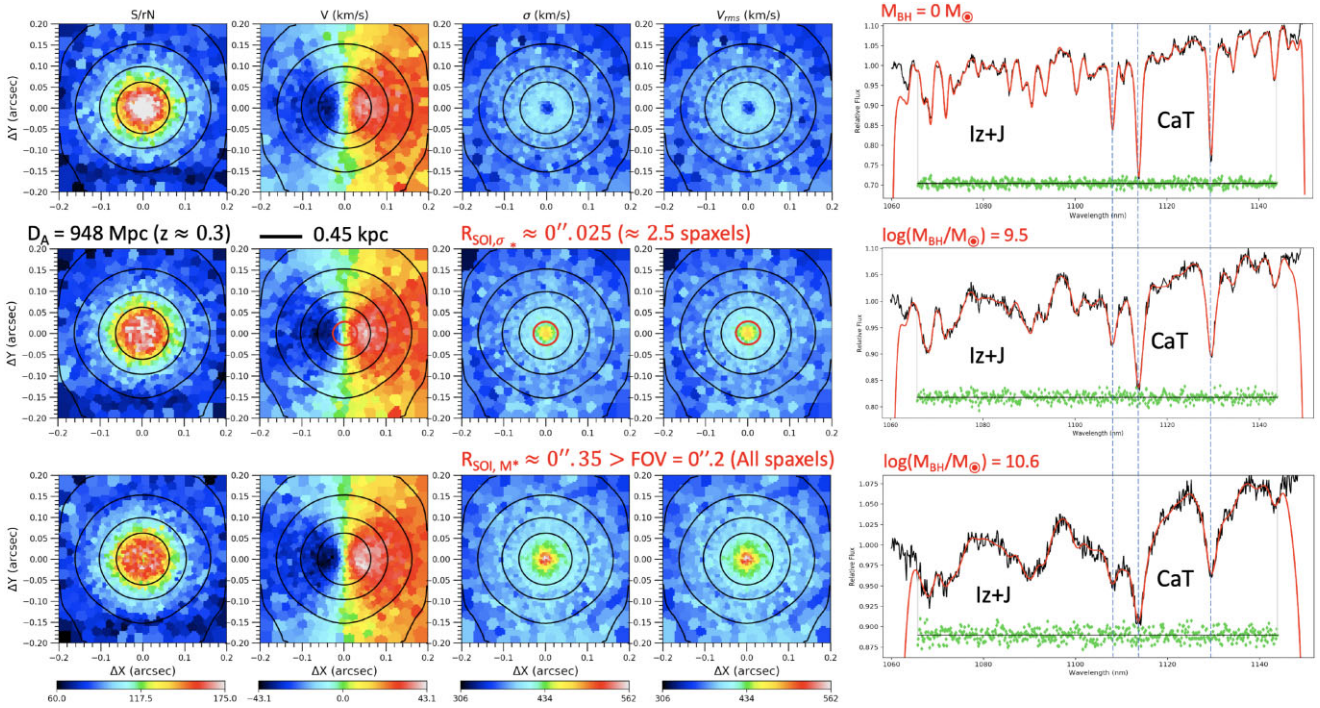

Figure 10. The stellar kinematic maps of 2MASXJ11480221+0237582 extracted from a spectral part (1.065 μm $< \lambda <$ 1.145 μm, $z \approx 0.3$), which contains the CaT stellar-absorption line (λ0.86–0.87 μm) of its mock $I_z + J$ HSIM IFS cubes produced from JAM_{sph} (Section 5.2) using PPXF. These maps are presented with three different black hole masses: $M_{\text{BH}} = 0$ $M_\odot$ (top row), 3×10^9 $M_\odot$ (middle row), and 4.4×10^{10} $M_\odot$ (bottom row). On each row, these maps are listed from left to right with (1) the signal-to-residual-noise ratio (S/rN) measuring the standard deviation of the residuals between the galaxy spectrum and the best-fitting PPXF model to define a residual noise (rN) for each Voronoi bin, (2) relative velocity (V), (3) velocity dispersion ($\sigma_\star$), (4) root-mean-squared velocity (V_{rms}), the black contours in all four maps indicating the isophotes from the collapsed HSIM IFS cubes spaced by 0.5 mag arcsec^{-2}, and (5) part of the simulated spectrum, showing the CaT-absorption features indicated by thin vertical dashed lines) of the stellar component extracted from one bin (black line) and its best-fitting model produced by PPXF (red line). Two grey vertical lines limit the wavelength range where the spectrum is fitted, and green dots show the residual between the galaxy spectrum and the best-fitting model (`data--model`). Colour bars at the bottom of the corresponding maps are fixed at the same scale for all three black hole masses to illustrate the kinematic effects of the central black holes and also indicate the robustness of our proposed kinematic measurements having at the centres of these highest-mass galaxies the kinematic signatures for SMBHs/MMBHs. The red circles at the centres of middle-row maps demonstrate the size of the SMBH SOI radius (R_{SOI}).

spectra and stellar model, we used the MARCS (Gustafsson et al. 2008) version of the Maraston & Strömbäck (2011) SPS models and default Legendre polynomials for correcting the template continuum shape (i.e. by setting `mdegree = 0, degree = 4`), and fit only for V and $\sigma_\star$ (i.e. by setting `moments = 2`). In addition, we also accounted for the HARMONI IFS instrumental broadening by broadening the stellar templates with the constant instrumental dispersion adopted by HSIM, which must be done before log-rebinning the spectra. In addition, to make our fit more realistic, we included 13 templates with ages from 3–15 Gyr and Solar metallicities (`z002`). The best-fitting SPS template was overlaid on the simulated spectra. Their residuals (`data--model`) are also shown simultaneously in the same panel to illustrate the quality of the fits.

We tested the usage of the $H + K$-band wavelength region, which is rarely used for kinematics studies (but see Crespo Gómez et al. 2021) (i.e. using some strongly stellar features but not using the CO-absorption bandheads because they fall out of the grating wavelength). Thus, we first tested with different chunks of wavelength ranges in the $H + K$ band, for example, the $H + K$ short (blue, 1.70–1.97 μm, which contains the atomic absorption Mg I λ1.487 μm) and $H + K$ long (red, 1.97–2.15 μm, which contains the atomic absorption Si I λ1.589 μm and the CO absorptions CO(3–0) λ1.540 μm, CO(4–1) λ1.561 μm, CO(5–2) λ1.577 μm, CO(6–3) λ1.602 μm, CO(7–4) λ1.622 μm, and CO(8–5) λ1.641 μm), and found they provide consistent kinematic maps. Note that these ranges of $H + K$ short and $H + K$ long are subject to change substantially depending on the redshift of the target. Next, we compared the kinematic results extracted from the $H + K$ band to those extracted from the stellar CaT features in the $I_z + J$ band. They prove that some of these strong stellar features in the $H + K$ grating to measure stellar kinematics are robust and feasible for measuring SMBH masses with minimum uncertainty.

The stellar kinematic maps shown in Figs 10 and 11 have central drops of $\sigma_\star$ and V_{rms} for the case of zero black holes that are consistent with our core-Sérsic most massive galaxies. The central drop in velocity dispersion is a general feature of the predicted stellar kinematics of galaxies without central SMBHs, for a range of assumed density and anisotropy profiles (e.g. Tremaine et al. 1994). Instead, models with an SMBH with the mass either following equation (2) or (3) of K18 create centrally raised peaks towards the galaxy centre in both the velocity dispersion and root-mean-squared velocity map. This fact agrees with the general expectation that the central velocity dispersion should be increased in a Keplerian way generally where the central SMBH's potential dominates (e.g. Tremaine et al. 1994). The difference between these kinematic maps at the galaxy centre is very clearly visible, especially for the cases with and without a central SMBH in 2MASXJ11480221+0237582, one of the farthest targets of our most massive survey sample, demonstrating the unprecedented

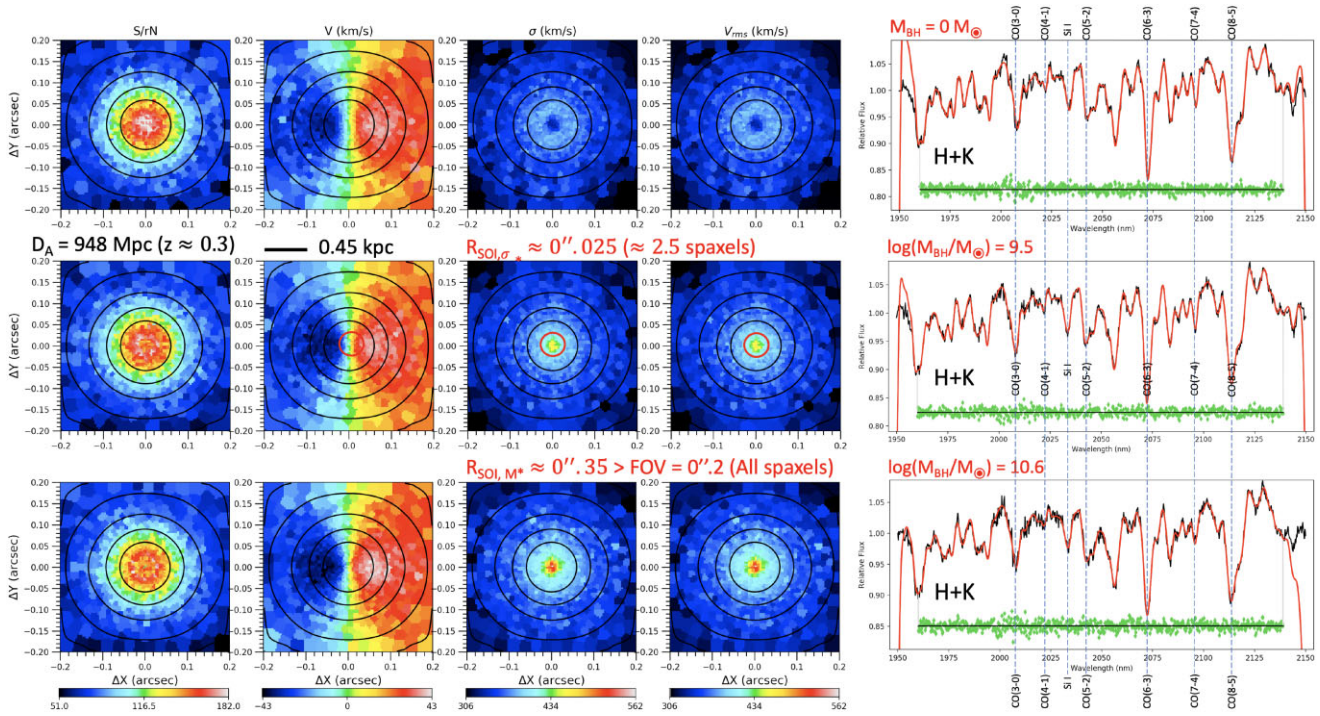

Figure 11. Same as Fig. 10 but for the galaxy 2MASXJ11480221+0237582 extracted from part of the strongest stellar-absorption features (1.955 μm < λ < 2.135 μm, $z \approx 0.3$; indicated by thin vertical dashed lines and labels) of its mock $H + K$ HSIM IFS cubes produced from JAM_{sph} using PPXF. This spectrum part contains a strong atomic absorption line (Si I λ1.589 μm) and some CO-absorption lines from the atmospheres of evolved giant stars and cool AGB stars: CO(3–0) λ1.540 μm, CO(4–1) λ1.561 μm, CO(5–2) λ1.577 μm, CO(6–3) λ1.602 μm, CO(7–4) λ1.622 μm, and CO(8–5) λ1.641 μm.

spectral and spatial resolving powers of ELT/HARMONI in detecting stellar kinematic signatures of central SMBHs at a large distance (e.g. out to a redshift of $z \leq 0.3$) and measuring their mass accurately and dynamically.

The edge effect is clearly visible on the kinematic maps, which always produces higher velocity dispersions (and thus higher root-mean-squared velocity) for the top and bottom bins (see the $\sigma_\star$ and V_{rms} maps in Figs 10 and 11) than their actual predictions of decreasing values because these spaxel bins are away from the centre. This effect also results in the squared shape for several of the outermost surface-brightness contours. To avoid any uncertainty due to this instrumental issue in our dynamical modellings, we exclude all these high-V_{rms} bins in our recovery models for the M_{BH} (Section 6.1).

The other eight chosen simulated galaxies (listed in Tables 3 and 4) with their kinematic results extracted from the $I_z/I_z + J$ and $H + K$ HSIM mock data cubes are shown side by side in Figs A1, A5, A9, A13, A17, A21, A25, and A29 of Appendix A (available as supplementary material) for comparison but excluding the PPXF fitting plots. We should note that the first four of these eight galaxies have low redshifts and their CaT features still stay in the wavelength range of the I_z grating (0.83–1.05 μm). We thus simulated their I_z observations instead of $I_z + J$ for a higher spectral resolution.

6 RESULTS

6.1 Black hole mass recovery

In Section 5, we used JAM_{sph} (C20) modelling to generate the 2D intrinsic first- and second-order velocity distributions of stellar kinematics (i.e. V and $\sigma_\star$), which were then used to convolve with the Maraston SPS models based on the MARCS library (Gustafsson et al. 2008, Section 4.2) to simulate the IFS data cubes and extract their corresponding kinematics maps (V, $\sigma_\star$, V_{rms}, Section 5.3). During this process, we assumed some dynamical parameters and hypotheses for a central compact dark mass object (M_{BH}), stellar orbitals (β_r), stellar mass (M/L_i), and inclination angle (i). In this section, we do a reversed process using the JAM_{sph} modelling itself and assume the available stellar kinematic measurements from our mock HARMONI IFS cubes (Section 5.3) to infer (or recover) these dynamical parameters, especially M_{BH}.

The JAM_{sph} model fits the simulated kinematics data with the following parameters: (1) inclination angle (i), (2) the mass of a point-like SMBH M_{BH}, (3) M/L_i, which parametrizes M/L relative to the best-fitting stellar population estimated in the i band, and (4) the global anisotropic parameter β_r among the population of stellar orbits ($\gamma = \beta_r$, implemented in Section 5.2). All four parameters are spaces on linear scales. Note that although we create synthetic models with anisotropy profiles that vary slightly with radius, the fitted model assumes a constant anisotropy for simplicity. JAM_{sph} generates kinematic models that can be compared with their corresponding simulated values (V_{rms}) within their errors. We also tested with the accurately known HSIM LTAO PSF of ELT/HARMONI, which has $\sigma_{\text{PSF}} \approx 5$ mas (or $\text{FWHM}_{\text{PSF}} \approx 12$ mas).

In JAM_{sph} modelling, we created a Markov chain Monte Carlo (MCMC) simulation to fully sample the parameter space of i, M/L_i, M_{BH}, and β_r. The model is used to fit the simulated kinematic data to find their best-fitting values and statistical uncertainties using the adaptive Metropolis algorithm (Haario, Saksman & Tamminen 2001) in the Bayesian framework (the ADAMET[14] package; Cappellari et al. 2013a). We ran our MCMC chains for the JAM_{sph} models with

[14] v2.0.9, available from https://pypi.org/project/adamet/

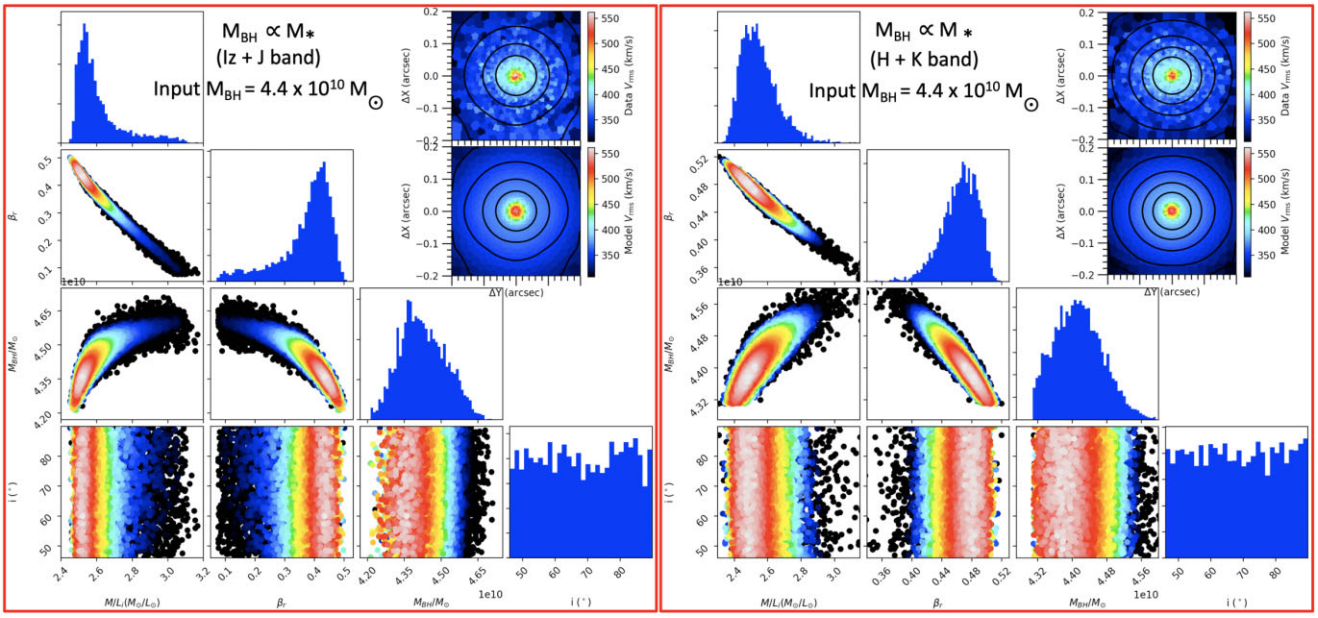

Figure 12. The ADAMET MCMC post-burn-in phase posterior distributions for our best-fitting JAM_{sph} models assuming a central black hole with a mass that follows the M_{BH}–$M_{\star}$ relation for galaxies with masses above M_{crit} predicted by equation (3) of K18 (see text for details). These posterior distributions were obtained when optimizing the JAM_{sph} models to the HSIM simulated kinematics of the galaxy 2MASXJ11480221+0237582 created using the JAM_{sph} models (Section 5.2). The scatter plots show the projected 2D distributions for each parameter. The histograms show the projected 1D distributions. From top left to bottom right, the panels show the inclination i, M_{BH}, M/L_i, and β_r for JAM_{sph}. The inset V_{rms} maps are the simulated kinematic maps extracted from the simulated data cubes (top), while the maps recovered from the best-fitting JAM_{sph} models (bottom) are shown to visually illustrate the agreements/disagreements at every spaxel between the simulated data and our adopted best-fitting model. These posteriors are produced using the $I_z + J$ (left) and $H + K$ (right) band HARMONI-simulated kinematics with $M_{\text{BH}} = 4.4 \times 10^{10}$ $\text{M}_{\odot}$; other input parameters are listed in Table 4.

a total of 3×10^4 calculations. We excluded the first 20 per cent of calculations as the burn-in phase to produce the full probability distribution function (PDF) from the 80 per cent remaining measures. The best-fitting parameters are the highest likelihood of the PDF.

As examples, we show in Figs 12–14 our best-fitting JAM_{sph} (Fig. 12 for input $M_{\text{BH}} = 4.4 \times 10^{10}$ $\text{M}_{\odot}$ predicted from equation (3) of K18, Fig. 13 for input $M_{\text{BH}} = 3 \times 10^9$ $\text{M}_{\odot}$ predicted from equation (2) of K18, and Fig. 14 for input $M_{\text{BH}} = 0$ $\text{M}_{\odot}$) parameters and their associated statistical uncertainties, respectively, that describe the corresponding simulated HARMONI IFS and the derived stellar kinematics of three different M_{BH} values for the galaxy 2MASXJ11480221+0237582 in two bands, $I_z + J$ and $H + K$, accordingly. Here, we use 2D distribution scatter plots for each parameter, with coloured points indicating their likelihood (white corresponds to the maximum likelihood and black to a confidence level smaller than 3σ). The histograms show the 1D distributions for each parameter. We used the 1D distributions to calculate the best-fitting values and their corresponding uncertainties, listed in Table 6.

To highlight the differences between the model and the data, we demonstrate in Fig. 15 the V_{rms} residual maps, `(data--model)/data`, produced from the upper and lower V_{rms} insets shown in Figs 12, 13, and 14 of the galaxy 2MASXJ11480221+0237582 (as an example representing all nine simulations), which show the relative agreements/disagreements from pixel to pixel of the V_{rms} maps. The considerable disagreements are all mostly minor, within 10 per cent, clearly seen in two regions with clear causes. The very central region ($r \lesssim 0.06$ arcsec) where we assumed an input anisotropy $\beta_r = -0.2$ (tangential) in the simulated IFS that is different from the main body's anisotropy ($\beta_r = +0.2$, radial), while in the recovery JAM_{sph} models we used a fixed anisotropy ($\beta_r =$ constant). The purpose of using a common anisotropy among the population of stellar orbits is for simplicity but allows us to obtain as good a fit as possible and speeds up the calculations, although this will not be done with the actual data. At larger radii ($r > 0.06$ arcsec), even though we have approximated the dynamics of core-Sérsic galaxies to be slow rotators and simulated the IFS with the JAM_{sph} model, some amount of rotation seems to have a significant contribution. The existence of a large rotation fraction in the kinematics (i.e. $V/\sigma \gtrsim 0.3$) can be seen with other galaxies in the figures in Appendix A (available as supplementary material): 2MASXJ22354078+0129053 (Fig. A1), 2MASXJ12052321+1022461 (Fig. A9), and 2MASXJ00034964+0203594 (Fig. A13). Although the differences are not sufficiently large to rule out the JAM_{sph} models, a large fraction of V/σ in some galaxies suggests that the use of JAM_{sph} instead of the Jeans equations, which assume axisymmetry with a cylindrically aligned orientation of the velocity ellipsoid (JAM_{cyl}; Cappellari 2008), is a relatively poor assumption.

Our models recovered the M_{BH} and M/L_i values very well and are close to the input values used when creating the input-noiseless cubes, which were supplied to the HSIM simulations for the HARMONI IFS. Specifically, these differences are $\lesssim 5$ per cent for both M_{BH} and M/L_i. For the uncertainties, we caution that these statistical errors found from the MCMC routines are formal and small (e.g. $3\sigma \approx 3$ per cent) because (1) our simulated kinematics are high quality and (2) the proposed black hole's SOI (i.e. $r_{\text{SOI}} \approx 20$ mas; Section 2.1) is totally resolvable with our HARMONI 10×10 mas^2 simulated angular scale. In fact, r_{SOI} depends on both M_{BH} and $\sigma_{\star}$, and therefore is different from galaxy to galaxy, as listed in Table 4 and indicated by the red circles in Figs 13 and 14 in the main text and Figs A1, A5, A9, A13, A17, A21, A25, A29 in Appendix A (available as

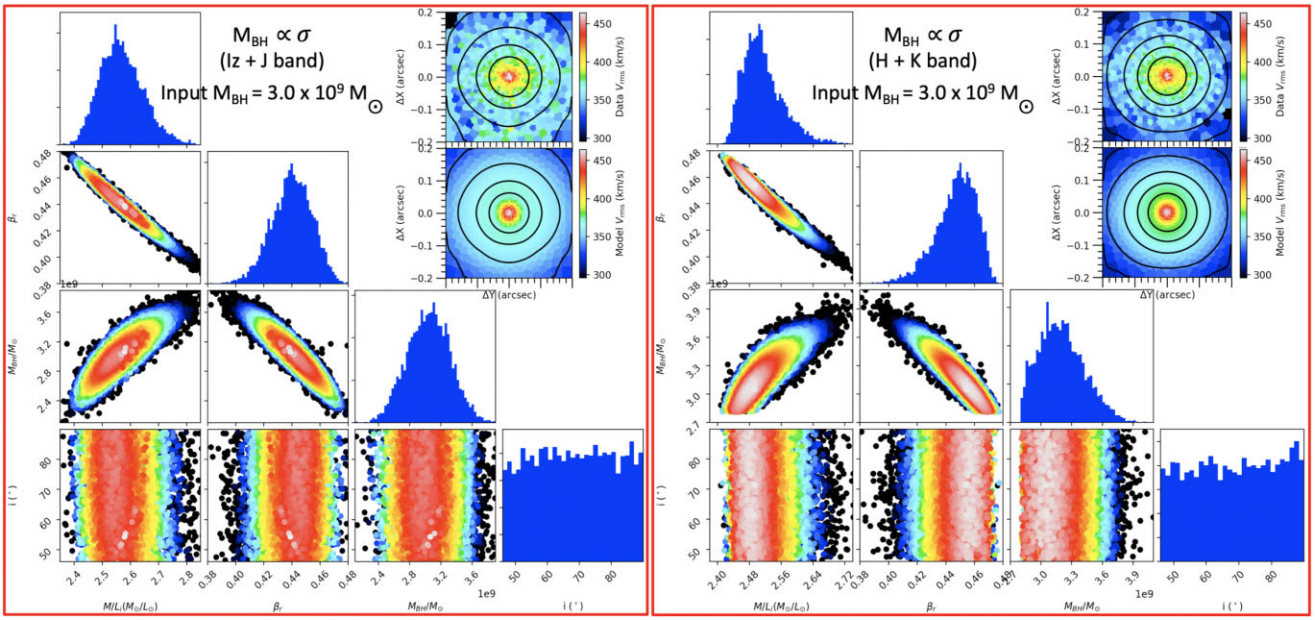

Figure 13. Same as Fig. 12 but for the HARMONI-simulated kinematics with $M_{\rm BH} = 3 \times 10^9$ M$_\odot$, which follows the $M_{\rm BH}$–$\sigma_\star$ relation for galaxies with masses below $M_{\rm crit}$ predicted by equation (2) of K18 for the galaxy 2MASXJ11480221+0237582.

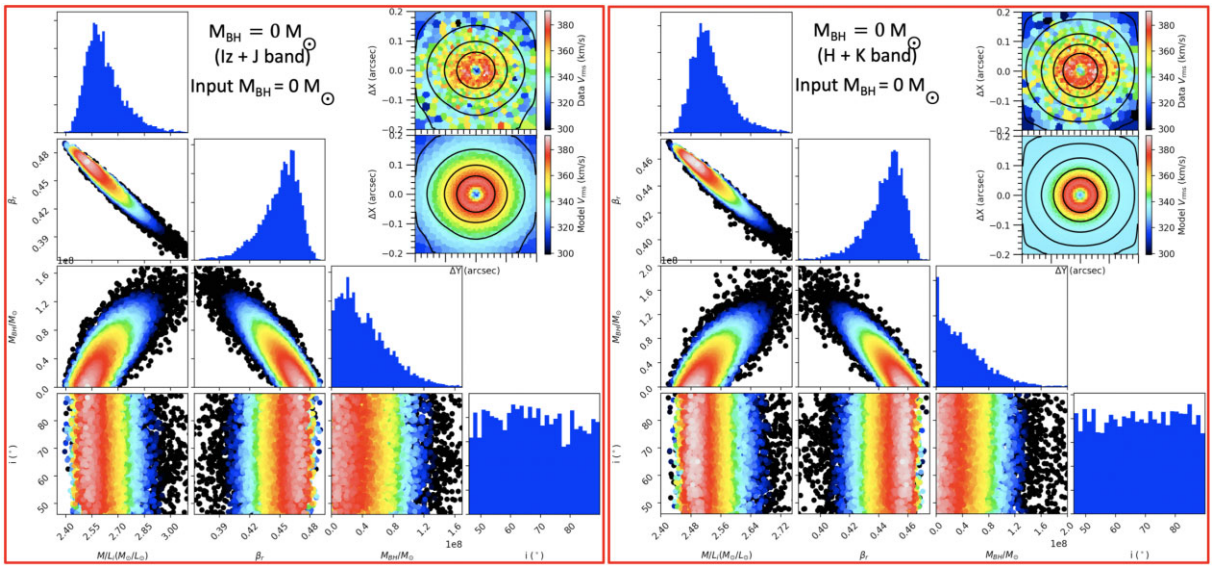

Figure 14. Same as Fig. 12 but for the HARMONI-simulated kinematics with $M_{\rm BH} = 0$ M$_\odot$ for the galaxy 2MASXJ11480221+0237582.

supplementary material), or by the text on the figure legends if the $r_{\rm SOI}$ values are larger than the simulated FOV. Graphically, a short summary of these black hole mass comparisons between the input values for HSIM and their corresponding recovered values using the ADAMET MCMC algorithm and JAM$_{\rm sph}$ modellings is also given in Fig. 16. We also show in this figure the recovered black hole masses for the other eight galaxies listed in Table 4 for sample completeness because we considered these nine galaxies to be representative of our MMBH survey sample.

In the cases of inputs $M_{\rm BH} = 3 \times 10^9$ M$_\odot$ and $M_{\rm BH} = 4.4 \times 10^{10}$ M$_\odot$, there seems to be a 'covariance' between $M_{\rm BH}$ and M/L_i due to the degeneracy between the potentials of the central black holes and the galaxies themselves, resulting in a 'banana' shape for the 3σ confidence levels in the 2D PDF found between these two parameters. However, this should not be the case because our simulated observational scale of 10×10 mas^2 is high enough for resolution within the central black hole's SOI even though this galaxy is at the upper limit of our MMBH survey sample's redshift range ($z \approx 0.3$; we remind ourselves that our proposed survey is at $r_{\rm SOI} \approx 20$ mas). In the meantime, we observe 'banana' shapes in the 2D PDFs of $M_{\rm BH}$ and M/L_i correlations (Figs 12 and 13), which follow a purely positive trend. This purely positive 'banana' shape also appears for the case of input $M_{\rm BH} = 0$ M$_\odot$ (Fig. 14), resulting in an upper limit for $M_{\rm BH}$. These $M_{\rm BH}$ values are smaller than the statistical errors of the two former cases due to the high angular and spectral resolutions of the simulated kinematic data.

In addition, we observe a variety of distribution trends for this 'banana' shape in Appendix A (available as supplementary mate-

Table 6. Best-fitting JAM$_{sph}$ parameters and their statistical uncertainties for the $I_z + J$- and $H + K$-band simulated kinematics of the 2MASXJ11480221+0237582 galaxy, the farthest one in our nine simulated targets.

Parameter name (1)	Search range of parameters (2)	Input value for HSIM (3)	Best-fitting value (4) $I_z + J$	1σ error (16–84 per cent) (5) $I_z + J$	3σ error (0.14–99.86 per cent) (6) $I_z + J$	Best-fitting value (7) $H + K$	1σ error (16–84 per cent) (8) $H + K$	3σ error (0.14–99.86 per cent) (9) $H + K$
Assuming no central SMBH ($M_{BH} = 0$ M$_\odot$)								
M_{BH}/M$_\odot$	$(0 \longrightarrow 10^{12})$	0	1.2×10^5	$\pm 3.5 \times 10^7$	$\pm 9 \times 10^7$	1.1×10^5	$<3.8 \times 10^7$	$<1.1 \times 10^8$
M/L_i (M$_\odot$/L$_\odot$)	$(0 \longrightarrow 10)$	2.5	2.52	± 0.11	± 0.43	2.50	± 0.05	± 0.26
i (°)	$(45 \longrightarrow 90)$	60.0	88.4	± 15.6	± 21.9	65.0	± 15.8	± 21.9
β_r	$(-15 \longrightarrow 1)$	± 0.2	0.47	± 0.02	± 0.07	0.46	± 0.01	± 0.06
Assuming a central SMBH with mass $M_{BH} = 3 \times 10^9$ M$_\odot$, derived from the M_{BH}–$\sigma_\star$ relation (equation 2 from K18)								
M_{BH}/M$_\odot$	$(0 \longrightarrow 10^{12})$	3.0×10^9	3.1×10^9	$\pm 3.0 \times 10^8$	$\pm 7.7 \times 10^8$	3.0×10^9	$\pm 2.5 \times 10^8$	$\pm 5.5 \times 10^8$
M/L_i (M$_\odot$/L$_\odot$)	$(0 \longrightarrow 10)$	2.5	2.58	± 0.08	± 0.24	2.50	± 0.05	± 0.15
i (°)	$(45 \longrightarrow 90)$	60.0	54.3	± 15.7	± 21.9	71.4	± 16.1	± 21.9
β_r	$(-15 \longrightarrow 1)$	± 0.2	0.44	± 0.02	± 0.04	0.45	± 0.02	± 0.04
Assuming a central SMBH with mass $M_{BH} = 4.4 \times 10^{10}$ M$_\odot$, derived from the M_{BH}–$M_\star$ relation (equation 3 from K18)								
M_{BH}/M$_\odot$	$(0 \longrightarrow 10^{12})$	4.4×10^{10}	4.4×10^{10}	$\pm 1.0 \times 10^9$	$\pm 2.3 \times 10^9$	4.4×10^{10}	$\pm 6.3 \times 10^8$	$\pm 1.4 \times 10^9$
M/L_i (M$_\odot$/L$_\odot$)	$(0 \longrightarrow 10)$	2.5	2.52	± 0.13	± 0.33	2.52	± 0.11	± 0.37
i (°)	$(45 \longrightarrow 90)$	60.0	59.9	± 15.9	± 21.9	85.8	± 16.0	± 21.9
β_r	$(-15 \longrightarrow 1)$	± 0.2	0.43	± 0.09	± 0.21	0.47	± 0.03	± 0.07

N otes. The table columns list each parameter name (column 1), search range (column 2), input value (column 3; the input value of β_r was discussed in Section 5.2), best fit (or upper limit), and uncertainty at the 1σ (16–84 per cent of the PDF) and 3σ (0.14–99.86 per cent of the PDF) confidence levels (columns 4, 5, 6 are the results obtained from the $I_z + J$ simulated kinematics, and columns 7, 8, 9 are the results obtained from the $H + K$ simulated kinematics). See also Fig. 16 for a graphically short summary of this table. The number 9 follows the target order in Tables 3 and 4.

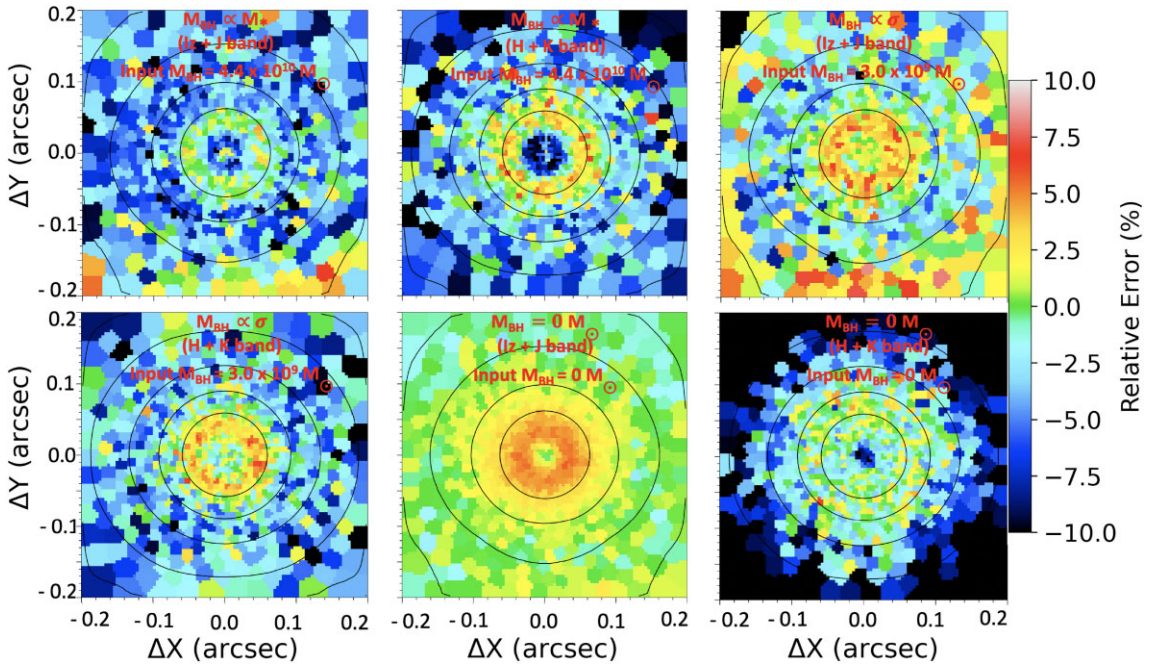

Figure 15. V_{rms} residual maps demonstrating the spatially relative agreements/disagreements between the HSIM simulated kinematic data and the best-fitting JAM$_{sph}$ model, `(data--model)/data`, of the galaxy 2MASXJ11480221+0237582, shown in the inset plots of Figs 12, 13, and 14. The corresponding information for input black holes and HSIM IFS bands is listed in the legend of each panel. All maps share a common colour bar on the right. Our best-fitting recovery JAM$_{sph}$ models fit the data well with the relative error <10 per cent for all cases across the simulated FOV of 0.4 × 0.4 arcsec.

rial), including purely positive (e.g. 2MASXJ13080241+0900044 in Figs A6, A7, and A8), purely close to zero (e.g. galaxy 2MASXJ09322275+0811508 in Figs A22, A23, and A24 and galaxy 2MASXJ10221610+0522524 in Figs A26, A27, and A28), and a mixture between positive, negative (or anticorrelation, which is usually expected in the covariance between M_{BH} and M/L_i in dynamical modellings), and close to zero (e.g. 2MASXJ22354078+0129053 in Figs A2, A3, and A4, 2MASXJ12052321+1022461 in Figs A10, A11, and A12, 2MASXJ00034964+0203594 in Figs A14, A15, and A16, 2MASXJ16171650+0638149 in Figs A18, A19, and A20, and 2MASXJ14155764+0318216 in Figs A30, A31, and A32) for kinematics extracted from the $I_z + J$ and $H + K$ IFS simulated

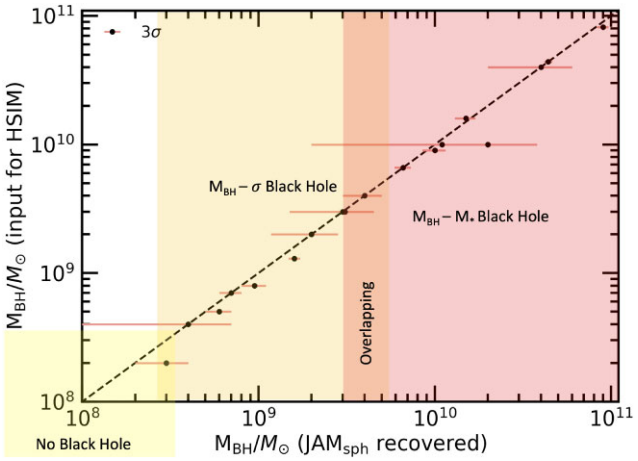

Figure 16. A summarized comparison of input black holes for HSIM and our recovered black holes (including statistical error bars at the 3σ confidential levels) using $\mathrm{JAM_{sph}}$ and IFS mock data cubes ($I_z/I_z + J$ and $H + K$) for all nine simulated galaxies (Table 4), which are listed in Tables 6, A1, A2, A3, A4, A5, A6, A7, and A8. The black dashed line is the equal-mass line between the input black hole masses for HSIM and our recovered black hole masses. The error bars of the recovered black hole masses are 3σ uncertainties (at the 0.14–99.86 percentiles) found from the MCMC fits of the $\mathrm{JAM_{sph}}$ modellings to the correspondingly simulated HSIM kinematic measurements (also listed in the tables mentioned above).

cubes. A possible – and the most likely – explanation for the lack of consistent anticorrelation between $M_{\rm BH}$ and M/L_i is that we used a spatially varying anisotropy, with tangential anisotropy near the central black holes, to generate the mock data with $\mathrm{JAM_{sph}}$, but then we applied a constant anisotropy to fit the data. This resulted in significant residuals and some unexpected positive correlations. This approach thus may not have been the best choice in retrospect. Another alternative reason for the existence of plenty of 2D PDF 'banana' shape is perhaps because the M/L_i parameter is not well constrained due to the small FOV or perhaps due to the systemic difference between models based on $I_z + J$ and $H + K$ kinematic extractions.

The recovery of β_r is also tightly constrained by the models, resulting in tiny uncertainties (see Figs 12, 13, and 14 and Table 6 for the galaxy 2MASXJ11480221+0237582). The preferred values of $\beta_r \approx (0.1\text{–}0.5)$ for $I_z + J$ and $\beta_r \approx (0.3\text{–}0.5)$ for $H + K$ (i.e. recovered β_r are dominated by $\beta_r > 0$ compared with their input $\beta_r = \pm 0.2$; see Section 5.2), respectively, suggesting that radial stellar orbits ($\beta_r > 0$) dominate. Something similar happens for the other eight galaxies with constrained ranges of β_r, as can be seen in the aforementioned figures in Appendix A (available as supplementary material).

As expected, we find that the inclination (i) is nearly unconstrained by the data. This is because, for all assumed inclinations, the modelled galaxies are by construction quite close to spherical, and in the spherical limit a galaxy looks the same from any inclination.

In Appendix A (available as supplementary material), we briefly discuss the other eight simulated targets with kinematic results and their black hole mass recovery and associated statistical uncertainties.

6.2 Sensitivity limits

Since we considered the nine most massive galaxies to be representative of our MMBH survey sample (Tables 3 and 4), their HARMONI IFS simulations at the pixel-sampling scale of $10 \times 10\,\mathrm{mas}^2$ in accurately determining stellar kinematics and dynamical $M_{\rm BH}$ measurements have demonstrated that the angular-size distances to the targets can be extended further than previous measurements ($\approx$100 Mpc; V16) up to a factor of $\approx$9 and $\approx$90 for $M_{\rm BH}$ predicted from equations (2) and (3) of K18, respectively. Thus, our proposed survey could push the current spatial-resolution limit of dynamical $M_{\rm BH}$ measurements and $M_{\rm BH}$ scaling relation evolution probes to redshift $z \leq 0.3$. In principle, this angular-size distance can be extended further up to a factor of five (i.e. accounting for the fact that we propose a survey at $r_{\rm SOI} = 20$ mas versus the highest spatial resolution of ELT, 4 mas). However, since the cosmological dimming effect limits the dynamical detections and measurements of SMBHs at further distances, these tasks must be ceased at a specific redshift. We will explore this limit in future work.

It is also worth testing the ultrasensitivity in terms of exposure time of the instruments for the same purposes. We repeated the same simulations for nine representative galaxies, decreasing the exposure times (and thus decreasing the spectral S/N) until the simulated HARMONI IFS cubes marginally provide meaningful kinematic maps after we bin the spaxels together via VORBIN with a specific bin S/N value of $\approx$25. This gives us the required exposure time for each galaxy in Column 4 of Table 5. Note that the galaxy's surface brightness was measured from the Pan-STARRS image and interpolated towards the regime of 10 mas using the core-Sérsic function in Section 4.3. In addition, we also considered the spread of flux along the grating wavelengths (Section 5.2). These required exposure times are relatively short, less than 45 min; they are thus suitable for ELT. Here, because of the lack of high-spatial-resolution imaging for precise surface-brightness measurements, we should caution that our sensitivity estimates in terms of exposure time only provide insight values for the MMBH survey. The real measurements of sensitivities are probably a bit higher (or have longer exposure times) because higher-spatial-resolution imaging (e.g. $\lesssim 0.05$ arcsec from *HST*/ACS and *JWST*/NIRCam or a few milliarcseconds from ELT/MICADO) will resolve some flux. We are thus demonstrating the possibility of our proposed science with ELT/HARMONI.

7 CONCLUSIONS

Given the purposes of exploring the stellar dynamics deep inside galaxy nuclei and weighing the central SMBHs, we investigated the potential applications of the unprecedented high-spatial-resolution and ultrasensitive observations offered by the ELT/HARMONI instrument. These are best for hunting for the most fundamental $M_{\rm BH}$–galaxy scaling relation (whether $M_{\rm BH}$–$\sigma_\star$ or $M_{\rm BH}$–$M_\star$) and can shed light on the physical processes from which we can derive the evolution picture between SMBHs and galaxies in a large sample of the most massive galaxies.

We defined such a complete sample ($z \leq 0.3$ and $M_K \leq -27.0$ mag) that is accessible at the location of ELT ($|\delta + 24^\circ| < 45^\circ$, $|b| > 8^\circ$). Our selection criteria are based on the mass selection ($K_{\rm s}$ band) of 2MRS assisted by NED-D, resulting in a sample of 101 highest-mass galaxies ($2 \times 10^{12} < M_\star \lesssim 5 \times 10^{12}\,\mathrm{M}_\odot$, statistically with 77 per cent ellipticals, 17 per cent lenticulars, and 7 per cent spirals). This sample extends to the locally largest-mass galaxies ($D_{\rm A} \leq 950$ Mpc) beyond currently well-known and large surveys of galaxies like $\mathrm{ATLAS^{3D}}$ (Cappellari et al. 2011), MASSIVE (Ma et al. 2014), and MaNGA (Graham et al. 2018), and similar to the M3G (Krajnović et al. 2018b) sample but including a wide range of environments from isolation to dense galaxy clusters. Our extensive survey of MMBHs is crucial for gaining insights into the mass buildup of the most massive galaxies. We achieve this through a comprehensive analysis of stellar and, if detectable, gas kinematics, photometric profiles,

and dynamical masses, all within the context of their respective environments. The HARMONI IFS observations of this MMBH sample will be compared against the modelling predictions to test formation scenarios and to develop the models at the top end of the galaxy-mass function. Thus, our limited redshift range ($z \approx 0.02$–0.3) survey is essential to investigate the evolution of global galaxy parameters with redshift and trace galaxy evolution back in time in combination and comparison with the availability of lower-redshift samples, i.e. ATLAS^{3D}, MaNGA, MASSIVE.

We tested the capacity of HARMONI IFS observations in measuring $M_{\rm BH}$ by doing the HSIM simulation for the I_z-, $I_z + J$-, and $H + K$-band IFS. For the I_z and $I_z + J$ gratings, we made use of the stellar absorption features of CaT (0.86–0.88 μm) to extract the simulated stellar kinematics. We also provided a guideline for using the $H + K$ IFS to obtain stellar kinematic measurements in the future. There are many strong stellar atomic absorptions (Mg I λ1.487 μm and Si I λ1.589 μm) and CO absorptions (CO(3–0) λ1.540 μm, CO(4–1) λ1.561 μm, CO(5–2) λ1.577 μm, CO(6–3) λ1.602 μm, CO(7–4) λ1.622 μm, and CO(8–5) λ1.641 μm). We found consistent kinematic maps extracted from the listed absorption features above within the instrument resolution ($\Delta V \lesssim 40\,{\rm km\,s^{-1}}$). We then used these data to estimate SMBH masses in combination with the interpolated stellar-mass model from the Pan-STARRS image and JAM$_{\rm sph}$ (C20) modellings. In this paper, we only tested the capability of the JAM$_{\rm sph}$ model to produce simulated HARMONI IFS cubes and recover the $M_{\rm BH}$ correspondingly from the simulated kinematic maps.

We found that the recovered $M_{\rm BH}$ and M/L_i from the simulated data are totally consistent with our input values (uncertainties $\lesssim$ 5 per cent) during the simulated process, although we made some different assumptions on the input and output anisotropy (input varying β_r versus output constant β_r). However, we should note that we did not compare the different JAM versions of the coordinate-aligned orientation of the velocity ellipsoid (spherical versus cylindrical, JAM$_{\rm cyl}$) in estimating the $M_{\rm BH}$ directly. Our simulations thus demonstrated that ELT/HARMONI will provide a unique facility for measuring SMBH mass and exploring the black hole mass–galaxy scaling relation evolution.

Our canonically proposed angular-resolution survey of $r_{\rm SOI} = 20 \times 20\,{\rm mas}^2$ with the simulated pixel scales of $10 \times 10\,{\rm mas}^2$ is high enough to resolve the stellar kinematics within the central black hole's SOI even though the galaxy is at the upper limit of our MMBH sample's redshift range ($z \approx 0.3$). The covariance between $M_{\rm BH}$ and M/L_i due to the degeneracy between the potentials of the central black holes and the galaxy itself should not be seen in the 3σ confidence levels in the 2D PDF. However, we observed a 'banana' shape in the posterior PDF of these two parameters with a variety of shapes, including purely positive, negative (anticorrelation), or a mixture between positive, negative, and close to zero for kinematics extracted from the $I_z + J$ and $H + K$ IFS simulated cubes. The reasons for the existence of plenty of 2D PDF 'banana' shapes and lack of anticorrelation may perhaps be that we used a spatially varying anisotropy (with tangential anisotropy near the SMBH) to generate the mock data with JAM$_{\rm sph}$, but then we applied a constant anisotropy to fit the data, which may not have been the best choice in retrospect. Alternatively, perhaps the M/L_i parameter was not well constrained due to the small FOV or the systemic difference between models based on $I_z + J$ and $H + K$ kinematic extractions.

Our simulations predict that within a relatively short observing time with ELT/HARMONI (i.e. less than one hour) one can obtain high-quality IFS and stellar kinematics data, demonstrating that HARMONI will be a cutting-edge instrument for investigating the above science goals.

ACKNOWLEDGEMENTS

The authors would like to thank the anonymous referee for his/her careful reading and useful comments, which helped to improve the paper greatly. DDN is grateful to the LABEX Lyon Institute of Origins (ANR-10-LABX-0066), Lyon, for its financial support within the programme 'Investissements d'Avenir' of the French government, operated by the National Research Agency (ANR). MPS acknowledges funding support from the Ramón y Cajal programme of the Spanish Ministerio de Ciencia e Innovación (RYC2021-033094-I).

The authors would like to thank Professor Joseph Jensen of the Department of Physics, Utah Valley University, for enlightening discussions on Pan-STARRS photometric calibration. We also thank some students of Vietnam National University in Ho Chi Minh City, Vietnam: the University of Natural Science (Ngo Ngoc Hai and Tong Gia Huy), the University of Technology (Le Nguyen Tuan), and the International University (Le Thong Quoc Tinh and On Tuan Phong) for their partial help with computation.

This research has made use of the NASA/IPAC Extragalactic Database (NED), which is operated by the Jet Propulsion Laboratory, California Institute of Technology, under contract with the National Aeronautics and Space Administration.

The Pan-STARRS1 Surveys (PS1) and the PS1 public science archive have been made possible through contributions by the Institute for Astronomy, the University of Hawaii, the Pan-STARRS Project Office, the Max Planck Society and its participating institutes, the Max Planck Institute for Astronomy, Heidelberg and the Max Planck Institute for Extraterrestrial Physics, Garching, the Johns Hopkins University, Durham University, the University of Edinburgh, the Queen's University Belfast, the Harvard-Smithsonian Center for Astrophysics, the Las Cumbres Observatory Global Telescope Network Incorporated, the National Central University of Taiwan, the Space Telescope Science Institute, the National Aeronautics and Space Administration under Grant No. NNX08AR22G issued through the Planetary Science Division of the NASA Science Mission Directorate, the National Science Foundation Grant No. AST-1238877, the University of Maryland, Eotvos Lorand University (ELTE), the Los Alamos National Laboratory, and the Gordon and Betty Moore Foundation.

Funding for SDSS-III has been provided by the Alfred P. Sloan Foundation, the Participating Institutions, the National Science Foundation, and the US Department of Energy Office of Science. The SDSS-III website is www.sdss3.org/. SDSS-III is managed by the Astrophysical Research Consortium for the Participating Institutions of the SDSS-III Collaboration including the University of Arizona, the Brazilian Participation Group, Brookhaven National Laboratory, Carnegie Mellon University, University of Florida, the French Participation Group, the German Participation Group, Harvard University, the Instituto de Astrofísica de Canarias, the Michigan State/Notre Dame/JINA Participation Group, Johns Hopkins University, Lawrence Berkeley National Laboratory, Max Planck Institute for Astrophysics, Max Planck Institute for Extraterrestrial Physics, New Mexico State University, New York University, Ohio State University, Pennsylvania State University, University of Portsmouth, Princeton University, the Spanish Participation Group, University of Tokyo, University of Utah, Vanderbilt University, University of Virginia, University of Washington, and Yale University. This publication makes use of data products from the Two Micron All Sky

Survey (https://old.ipac.caltech.edu/2mass/), which is a joint project of the University of Massachusetts and the Infrared Processing and Analysis Center/California Institute of Technology, funded by the National Aeronautics and Space Administration and the National Science Foundation.

Facilities: Pan-STARRS DR1 and DR2, SDSS DR12, 2MASS, and *HST*

Software: PYTHON 3.10 (https://www.python.org/), MATPLOTLIB 3.6.0 (https://matplotlib.org/), NUMPY 1.22 (https://www.scipy.org/install.html), SCIPY 1.3.1 (https://www.scipy.org/install.html), PHOTUTILS 0.7 (https://photutils.readthedocs.io/en/stable//), MPFIT (http://purl.com/net/mpfit), PLOTBIN 3.1.3 (https://pypi.org/project/plotbin/), ASTROPY 5.1 (Astropy Collaboration 2022), ADAMET 2.0.9 (Cappellari et al. 2013a), JAMPY 6.4.0 (Cappellari 2008, C20), PPXF 8.2.1 (Cappellari 2022), VORBIN 3.1.5 (Cappellari & Copin 2003), MGEFIT 5.0.14 (Cappellari 2002), and HSIM 3.10 (Zieleniewski et al. 2015).

DATA AVAILABILITY

All data and software used in this paper are public. We have provided links to them in the text when discussed. The data produced underlying this article will be shared on reasonable request to the corresponding author.

REFERENCES

Anglés-Alcázar D., Özel F., Davé R., 2013, ApJ, 770, 5
Astropy Collaboration, 2022, ApJ, 935, 167
Begelman M. C., Blandford R. D., Rees M. J., 1980, Nature, 287, 307
Bell E. F., de Jong R. S., 2001, ApJ, 550, 212
Bilir S., Ak S., Karaali S., Cabrera-Lavers A., Chonis T. S., Gaskell C. M., 2008, MNRAS, 384, 1178
Böker T., Falcón-Barroso J., Schinnerer E., Knapen J. H., Ryder S., 2008, AJ, 135, 479
Boylan-Kolchin M., Ma C.-P., Quataert E., 2006, MNRAS, 369, 1081
Bundy K. et al., 2015, ApJ, 798, 7
Calabrese E. et al., 2017, Phys. Rev. D, 95, 063525
Cappellari M., 2002, MNRAS, 333, 400
Cappellari M., 2008, MNRAS, 390, 71
Cappellari M., 2013, ApJ, 778, L2
Cappellari M., 2016, ARA&A, 54, 597 (C16)
Cappellari M., 2020, MNRAS, 494, 4819 (C20)
Cappellari M., 2022, preprint (arXiv:2208.14974)
Cappellari M., Copin Y., 2003, MNRAS, 342, 345
Cappellari M. et al., 2008, in Bureau M., Athanassoula E., Barbuy B.eds, Proc. IAU Symp. 245, Formation and Evolution of Galaxy Bulges. p. 215, preprint (arXiv:0709.2861), Cambridge University Press.
Cappellari M. et al., 2011, MNRAS, 413, 813
Cappellari M. et al., 2013a, MNRAS, 432, 1709
Cappellari M. et al., 2013b, MNRAS, 432, 1862
Cardelli J. A., Clayton G. C., Mathis J. S., 1989, ApJ, 345, 245
Chambers K. C. et al., 2016, preprint (arXiv:1612.05560)
Charlot S., Fall S. M., 2000, ApJ, 539, 718
Chilingarian I. V., Katkov I. Y., Zolotukhin I. Y., Grishin K. A., Beletsky Y., Boutsia K., Osip D. J., 2018, ApJ, 863, 1
Ciotti L., Bertin G., 1999, A&A, 352, 447
Crespo Gómez A., Piqueras López J., Arribas S., Pereira-Santaella M., Colina L., Rodríguez del Pino B., 2021, A&A, 650, A149
Crook A. C., Huchra J. P., Martimbeau N., Masters K. L., Jarrett T., Macri L. M., 2007, ApJ, 655, 790
Crook A. C., Huchra J. P., Martimbeau N., Masters K. L., Jarrett T., Macri L. M., 2008, ApJ, 685, 1320
Croom S. M. et al., 2021, MNRAS, 505, 991
Dallier R., Boisson C., Joly M., 1996, A&AS, 116, 239
Dametto N. Z., Riffel R., Pastoriza M. G., Rodríguez-Ardila A., Hernandez-Jimenez J. A., Carvalho E. A., 2014, MNRAS, 443, 1754
Davies R. et al., 2010, in McLean I. S., Ramsay S. K., Takami H.eds, Proc. SPIE Conf. Ser. Vol. 7735, Ground-based and Airborne Instrumentation for Astronomy III. SPIE, Bellingham, p. 77352A
Demorest P. B. et al., 2013, ApJ, 762, 94
Dullo B. T., 2019, ApJ, 886, 80
Emsellem E., Monnet G., Bacon R., 1994, A&A, 285, 723
Faber S. M. et al., 1997, AJ, 114, 1771
Ferrarese L., 2002, ApJ, 578, 90
Ferrarese L., Merritt D., 2000, ApJ, 539, L9
Förster Schreiber N. M., 2000, AJ, 120, 2089
García-Lorenzo B., Monreal-Ibero A., Mediavilla E., Pereira-Santaella M., Thatte N., 2019, Frontiers Astron. Space Sci., 6, 73
Gebhardt K. et al., 2000, ApJ, 539, L13
Gourgoulhon E., Le Tiec A., Vincent F. H., Warburton N., 2019, A&A, 627, A92
Graham A. W., Spitler L. R., 2009, MNRAS, 397, 2148
Graham A. W., Erwin P., Caon N., Trujillo I., 2001, ApJ, 563, L11
Graham A. W., Erwin P., Trujillo I., Asensio Ramos A., 2003, AJ, 125, 2951
Graham M. T. et al., 2018, MNRAS, 477, 4711
Greene J.E. et al., 2010, ApJ, 721, 26
Greene J. E. et al., 2016, ApJ, 826, L32
Greene J. E., Strader J., Ho L. C., 2020, ARA&A, 58, 257
Gültekin K. et al., 2009, ApJ, 698, 198
Gustafsson B., Edvardsson B., Eriksson K., Jørgensen U. G., Nordlund Å., Plez B., 2008, A&A, 486, 951
Haario H., Saksman E., Tamminen J., 2001, Bernoulli, 7, 223
Hirschmann M., Khochfar S., Burkert A., Naab T., Genel S., Somerville R. S., 2010, MNRAS, 407, 1016
Huchra J. P. et al., 2012, ApJS, 199, 26
Jahnke K. et al., 2011, ApJ, 734, 92
Jarrett T. H., Chester T., Cutri R., Schneider S. E., Huchra J. P., 2003, AJ, 125, 525
Jedrzejewski R. I., 1987, MNRAS, 226, 747
Jensen J. B., Blakeslee J. P., Gibson Z., Lee H.-c., Cantiello M., Raimondo G., Boyer N., Cho H., 2015, ApJ, 808, 91
Jensen J. B. et al., 2021, ApJS, 255, 21
Jones L. R., Ponman T. J., Horton A., Babul A., Ebeling H., Burke D. J., 2003, MNRAS, 343, 627
Kleinmann S. G., Hall D. N. B., 1986, ApJS, 62, 501
Kormendy J., Bender R., 1996, ApJ, 464, L119
Kormendy J., Bender R., 2009, ApJ, 691, L142
Kormendy J., Ho L.C., 2013, ARA&A, 51, 511
Kormendy J., Richstone D., 1995, ARA&A, 33, 581
Kotilainen J. K., Hyvönen T., Reunanen J., Ivanov V. D., 2012, MNRAS, 425, 1057
Krajnović D. et al., 2013, MNRAS, 432, 1768
Krajnović D., Cappellari M., McDermid R. M., 2018a, MNRAS, 473, 5237 (K18)
Krajnović D., Emsellem E., den Brok M., Marino R. A., Schmidt K. B., Steinmetz M., Weilbacher P. M., 2018b, MNRAS, 477, 5327
Läsker R. et al., 2016, ApJ, 825, 3
Lauer T.R., Läsker R. et al., 2007a, ApJ, 662, 808
Lauer T. R. et al., 2007b, ApJ, 664, 226
Lavaux G., Hudson M. J., 2011, MNRAS, 416, 2840
Li H. et al., 2017, ApJ, 838, 77
Lupton R. H., Gunn J. E., Szalay A. S., 1999, AJ, 118, 1406
Ma C.-P. et al., 2014, ApJ, 795, 158
Magnier E. A. et al., 2020, ApJS, 251, 5
Magorrian J. et al., 1998, AJ, 115, 2285
Maraston C., 2005, MNRAS, 362, 799
Maraston C., Strömbäck G., 2011, MNRAS, 418, 2785
Markwardt C. B., 2009, in Bohlender D. A., Durand D., Dowler P.eds, ASP Conf. Ser. Vol. 411, Astronomical Data Analysis Software and Systems XVIII. Astron. Soc. Pac., San Francisco, p. 251
McConnell N. J., Ma C.-P., 2013, ApJ, 764, 184

McConnell N. J., Ma C.-P., Gebhardt K., Wright S. A., Murphy J. D., Lauer T. R., Graham J. R., Richstone D. O., 2011a, Nature, 480, 215
McConnell N. J., Ma C.-P., Graham J. R., Gebhardt K., Lauer T. R., Wright S. A., Richstone D. O., 2011b, ApJ, 728, 100
McConnell N.J. et al., 2012, ApJ, 756, 179
McConnell N.J. et al., 2013, ApJ, 764, 184
Mitzkus M., Cappellari M., Walcher C. J., 2017, MNRAS, 464, 4789
Mulchaey J. S., Jeltema T. E., 2010, ApJ, 715, L1
Naab T., Ostriker J. P., 2017, ARA&A, 55, 59
Nguyen D. D., Improved dynamical constraints on the mass of the central black hole in NGC 404, 2017, ApJ, 836, 237, https://ui.adsabs.harvard.edu/abs/2017arXiv171202470N. preprint (arXiv:1712.02470)
Nguyen D., 2019, in ALMA2019: Science Results and Cross-Facility Synergies, Uncovering the Census of Black Holes in sub-Milky Way Mass Galaxies. p. 106, https://zenodo.org/record/3585410#.ZR_Y1-xBzzh @ misc
Nguyen D. D., Seth A. C., Reines A. E., den Brok M., Sand D., McLeod B., 2014, ApJ, 794, 34
Nguyen D.D. et al., 2017, ApJ, 836, 237
Nguyen D.D. et al., 2018, ApJ, 858, 118
Nguyen D.D. et al., 2019, ApJ, 872, 104
Nguyen D. D. et al., 2020, ApJ, 892, 68
Nguyen D. D. et al., 2021, MNRAS, 504, 4123
Nguyen D. D. et al., 2022, MNRAS, 509, 2920
Oke J. B., 1974, ApJS, 27, 21
Oser L. et al., 2010, ApJ, 725, 2312
Peng C. Y., 2007, ApJ, 671, 1098
Peng C. Y., Ho L. C., Impey C. D., Rix H.-W., 2010, AJ, 139, 2097
Planck Collaboration, 2014, A&A, 571, A16
Roediger J.C. et al., 2015, MNRAS, 452, 3209
Rusli S. P., Thomas J., Erwin P., Saglia R. P., Nowak N., Bender R., 2011, MNRAS, 410, 1223
Rusli S. P., Erwin P., Saglia R. P., Thomas J., Fabricius M., Bender R., Nowak N., 2013, AJ, 146, 160
Saglia R.P. et al., 2016, ApJ, 818, 47
Sahu N., Graham A. W., Davis B. L., 2019a, ApJ, 876, 155
Sahu N., Graham A. W., Davis B. L., 2019b, ApJ, 887, 10
Schlafly E. F., Finkbeiner D. P., 2011, ApJ, 737, 103
Schombert J., Smith A. K., 2012, Publ. Astron. Soc. Australia, 29, 174
Schwarzschild M., 1979, ApJ, 232, 236
Scott N. et al., 2013, ApJ, 768, 76
Sersic J. L., 1968, Atlas de Galaxias Australes, https://ui.adsabs.harvard.edu/abs/1968adga.book.....S
Shannon R. M. et al., 2013, Science, 342, 334
Silge J. D., Gebhardt K., 2003, AJ, 125, 2809
Skrutskie M.F. et al., 2006, AJ, 131, 1163
Smith M. D. et al., 2020, MNRAS, 500, 1933
Steer I. et al., 2017, AJ, 153, 37
Sun A.-L., Greene J. E., Impellizzeri C. M. V., Kuo C.-Y., Braatz J. A., Tuttle S., 2013, ApJ, 778, 47
Thatte N. A. et al., 2016, in Proc. SPIE Conf. Ser. Vol. 9908, Ground-based and Airborne Instrumentation for Astronomy VI. SPIE, Bellingham, p. 99081X
Thatte N. A. et al., 2020, in Proc. SPIE Conf. Ser. Vol. 11447, Ground-based and Airborne Instrumentation for Astronomy VIII. SPIE, Bellingham, p. 114471W
Thomas J. et al., 2014, ApJ, 782, 39
Tremaine S., Richstone D. O., Byun Y.-I., Dressler A., Faber S. M., Grillmair C., Kormendy J., Lauer T. R., 1994, AJ, 107, 634
Trujillo I., Erwin P., Asensio Ramos A., Graham A. W., 2004, AJ, 127, 1917
van den Bosch R.C.E. et al., 2012, Nature, 491, 729
van den Bosch R. C. E., 2016, ApJ, 831, 134 (V16)
van Dokkum P. G. et al., 2015, ApJ, 813, 23
van Haasteren R. et al., 2011, MNRAS, 414, 3117
Wallace L., Hinkle K., 1997, ApJS, 111, 445
Walsh J. L., Barth A. J., Ho L. C., Sarzi M., 2013, ApJ, 770, 86
Walsh J.L. et al., 2015, ApJ, 808, 183
Walsh J.L. et al., 2016, ApJ, 817, 2
Walsh J.L. et al., 2017, ApJ, 835, 208
Waters C. Z. et al., 2020, ApJS, 251, 4
Wright E. L., 2006, PASP, 118, 1711
Zieleniewski S., Thatte N., Kendrew S., Houghton R. C. W., Swinbank A. M., Tecza M., Clarke F., Fusco T., 2015, MNRAS, 453, 3754

SUPPORTING INFORMATION

Supplementary data are available at *MNRAS* online.

Supplementary.pdf

Please note: Oxford University Pressis notresponsible forthe content or functionality of any supporting materials supplied by the authors. Any queries (other than missing material) should be directed to the corresponding author for the article.

This paper has been typeset from a TEX/LATEX file prepared by the author.